MEASUREMENT OF 18650 FORMAT LITHIUM ION BATTERY VENT MECHANISM FLOW PARAMETERS

by

FRANK AUSTIN MIER

Submitted in Partial Fulfillment
of the Requirements for the Degree of
Master of Science in Mechanical Engineering
with Specialization in Explosives Engineering

New Mexico Institute of Mining and Technology
Socorro, New Mexico
May, 2018

ABSTRACT

Lithium ion batteries have a well documented tendency to fail energetically under various abuse conditions. These conditions frequently result in decomposition reactions within the electrochemical components of the battery resulting in gas generation and increased internal pressure, which could lead to an explosive case rupture. The 18650 format cell incorporates a vent mechanism located within a crimped cap to relieve pressure and mitigate the risk of case rupture. However, cell venting introduces additional safety concerns associated with the flow of flammable gases and liquid electrolyte into the ambient environment. Experiments are performed here to quantify key parameters in describing the external dynamics of battery venting. A first experiment measures the vent burst pressure. Burst vent caps are then tested on a second experimental fixture developed to simulate the choked flow present during failures. This experiment allows measurement of the vent opening area and flow discharge coefficient from stagnation temperature, stagnation pressure, and static pressure measurements combined with a known fixture geometry, compressible-isentropic flow equations, and conservation of mass. Validation experiments are performed to confirm the accuracy of opening area and discharge coefficient measurement. A test series of fifty commercially sourced vent caps describes statistical characteristics of the measurements, and additional trials are performed on vent caps removed from live batteries to demonstrate the potential variation between manufacturers.

Keywords: Lithium ion battery; Safety; Venting failure; Burst pressure; Opening area; Discharge coefficient

ACKNOWLEDGMENTS

CONTENTS

LIST OF TABLES

LIST OF FIGURES

This thesis is accepted on behalf of the faculty of the Institute by the following committee:

<div style="text-align:center">

Michael J. Hargather
_____
Advisor

Jamie Kimberley
_____

Summer R. Ferreira
_____

</div>

I release this document to the New Mexico Institute of Mining and Technology.

_____

FRANK AUSTIN MIER   Date

CHAPTER 1

INTRODUCTION

1.1   Research motivation

Lithium ion batteries have the ability to fail energetically when subjected to conditions outside of the intended usage environment. The most dangerous and popularized battery failures are often associated with risks of flammability. Timelines of high profile battery failures show a persistent and ongoing need to mitigate risks [1]. By understanding the failure process, risks can be better assessed thus leading to improved safety in all applications of lithium ion batteries.

1.2   Lithium ion battery technologies and abuse testing

Conditions which can lead to battery failures include overcharge, over-discharge, high temperature, low temperature, over-current, internal defects, mechanical loading (shock, crush, and penetration), and age [2]. Abuse conditions generally initiate a rise in temperature which drives exothermic reactions within the cell. If these reactions become self sustaining, the battery is said to be in thermal runaway [3]. Experiments have shown that the onset of thermal runaway generally occurs below 125 °C [4]. These conditions can become a safety concern when the failure is not able to be contained within the cell and a venting event occurs. The primary diver behind cell venting is the generation of gases internal to the cell. Oxygen gas is generated at the cathode of common cell chemistries including lithium-cobalt-oxide (LCO), nickel-cobalt-aluminum (NCA), and nickel-manganese-cobalt (NMC) [5]. Reactions within the electrolyte can lead to generation of hydrocarbons which are flammable and increase pressure within the cell [3]. The combination of oxygen and hydrocarbons creates a scenario where combustion is possible regardless of the atmospheric composition.

Safety mechanisms are designed and fabricated into lithium ion batteries to mitigate the potential for catastrophic failures at the cell level. Current interrupt devices (CID) electrically disconnect the electrochemical components of a battery from external circuitry if conditions within the cell present high venting failure risk [6]. Cylindrical batteries usually have a current interrupt device which physically breaks an electrical connection when significant pressure is applied to a diaphragm which renders the battery permanently disconnected from

1

external circuits [7]. Positive temperature coefficient (PTC) elements are components which increase in electrical resistance at elevated temperatures. Generally located at a terminal, a PTC can effectively prevent current flow into or out of a battery, and thus provides good protection from electrical abuse conditions. Similar to the PTC, thermal fuses can be used to permanently disconnect a battery from external circuits at elevated temperatures. Further, while technically being a material failure within the battery, the phenomena of separator shutdown can act as a passive safety element to protect against high internal cell temperatures. Separator shutdown blocks ion transport when the temperature is higher than the melting point of the polymer separator effectively stopping additional charging or discharge. However, if temperature continues to rise, large holes in the separator can form and lead to energetic failures as an internal short circuit is created [8].

General testing procedures have been created to provide abuse testing guidelines for lithium ion battery abuse testing under the United States Advanced Battery Consortium [9]. These guidelines provide comparison between cells, and a baseline for more specialized tests.

Thermal abuse testing is often performed when evaluating the thermal runaway process, chemical composition of vented material, or flammability risk of a given cell. The 18650 format cell is often used in laboratory scale calorimetry where the relations between state of charge (SOC), calorimeter pressure, peak temperature, and test duration are compared. In general, experiments have shown increased calorimeter pressures, peak temperature, and minimized test duration as SOC is increased [10]. Calorimetry experiments have been used to subject cells to extreme conditions with failure modes such as "jelly roll" ejection where the vent completely fails and the electrochemical components of the battery exit the case [11]. Cone calorimetry tests on LCO 18650 cells have been used for sampling of vented material throughout thermal abuse testing which showed increased concentrations of vented carbon monoxide and carbon dioxide for cells at higher initial SOC [12]. Imaging within cells during thermal abuse testing has been achieved by real time CT scanning. When coupled with infrared imaging of the surface of an 18650 cell, internal failure was noted to correspond with a hot spot on the outside of the battery case [13].

In mechanical abuse tests, initial failures are highly localized via an internal short within the battery. CT imaging has been used after testing on 18650 cells subjected to blunt rod and nail penetration tests which clearly show internal shorts [14]. However, mechanical abuse testing on larger cells has suggested that torsion is a weakness within cell construction beyond the traditional penetration tests [15].

With the interest in developing safer cathode chemistries, lithium iron phosphate (LFP) cell chemistries have been extensively evaluated. LFP cells are more thermally stable than metal oxide chemistries and have a flatter discharge voltage curve, but they have a lower nominal voltage which is a challenge to accommodate in portable power applications [16]. In thermal abuse testing of LFP cells, there was less heat generation measured when compared to LCO [17].

Other thermal runaway experiments showed that like LCO and NMC cells, LFP battery venting contained hydrogen gas [18]. Lithium iron phosphate (LFP) cells have been tested at various SOC values where the venting of hydrocarbons was measured. In the presence of an ignition source, this vented material had a high likelihood of combusting [19]. In other experiments, thermal abuse tests on LFP have implemented Fourier Transform-Infrared Spectroscopy (FTIR) which measured potentially dangerous levels of hydrogen fluoride gas [20]. While LFP cells are generally considered more safe than metal oxide based batteries, there are still serious flammability risks involved. Some research has gone into moving towards a sodium based chemistry (Na_xFePO_4F) which has been demonstrated as cost effective and less hazardous than current chemistries [21].

Most applications of lithium batteries require multiple individual cells to be arranged into a larger pack based on voltage, current, and capacity demands. Experiments performed on battery packs have generally been similar to those performed on single cells. Examples include thermal abuse via fire testing which led to venting and combustion of vented material [22]. Additional research has included chemical analysis of vented material via FTIR [23]. Experiments have also been performed to demonstrate the propagation of failure from one cell to others in a battery back. Cascading battery failures occur as a cell in thermal runaway can be the source of thermal abuse to adjacent cells in the pack [24]. In these tests, cylindrical cells have shown reduced risk of failure propagation than pouch cells because less efficient heat transfer between cells [25]. To mitigate risks in battery packs development has gone into evaluating air cooling, liquid cooling, and inclusion of a phase change material between cells [26, 27, 28].

While extensive work has been performed on understanding the relative risks of different cell chemistries and how broadly different battery pack configurations respond to abuse, a detailed analysis of how individual features in the construction of the ubiquitous 18650 format battery relate to battery failure characteristics has not yet been performed. Constraints have been applied when analyzing battery venting including a stated burst pressure of 3,448 kPa [29]. This has been further applied to model the venting process from 18650 cells using isentropic flow equations and an initially choked flow [30]. However, expanding the level to which venting parameters are quantified will assist the evaluation of battery failures regardless of abuse condition or cell chemistry.

High-speed schlieren imaging was used to observe the external dynamics of lithium ion battery venting under thermal abuse and overcharge from multiple cell formats and chemistries as shown in Figure 1.1 [31]. Battery voltage, current, and case temperature were recorded simultaneously with high speed imaging. Schlieren imaging visualizes refractive index gradients which correspond to density gradients in gas and different chemical species [32].
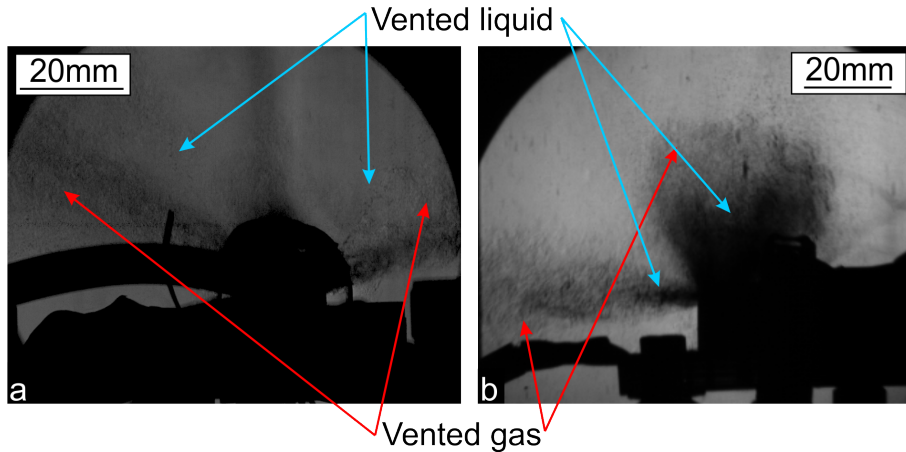
Figure 1.1: (a) Axial and (b) side view schlieren images of a LG MG1 (NMC) battery venting after being heated with two cartridge heaters placed adjacent to the outer battery case. These heaters were electrically powered at a rate of 75 W.

1.3 Details of the 18650 format lithium ion battery

1.3.1 Basic anatomy

In typical lithium ion battery construction, an anode, cathode, and separator are tightly wound and placed inside the battery case along with a liquid electrolyte. As shown in Figure 1.2, the positive terminal of the cell is crimped in place at the end of the cell. While not explicitly shown in Figure 1.2, safety features located at this terminal include the burst disk and vent, positive temperature coefficient (PTC) element, and current interrupt device (CID) which is connected to the cathode via a foil tab [7]. The foil tab is connected to the vent cap at a perforated plate which generally has varied geometry based on the manufacturer of the cell. Aside from to being referred to as a vent cap in this study, this assembly is sometimes called an "Anti-Explosive Cap" [33]. While designed with safety measures to combat the effects of abuse conditions, thermal runaway can still occur in some instances. If the pressure within the cell becomes too great, these vent caps are the components intended to fail in order to prevent complete case rupture or explosions.

1.3.2 Vent cap removal process

Vent caps are tested separately from the battery to create a more controlled experiment. To prevent damage of the vent cap and internal components of the cells, a pipe cutter was used to cut the battery case along the crimp line which mostly separates the vent from the electrochemical components of the cell. Separation is completed when electrical snips were used to cut the foil tab between the
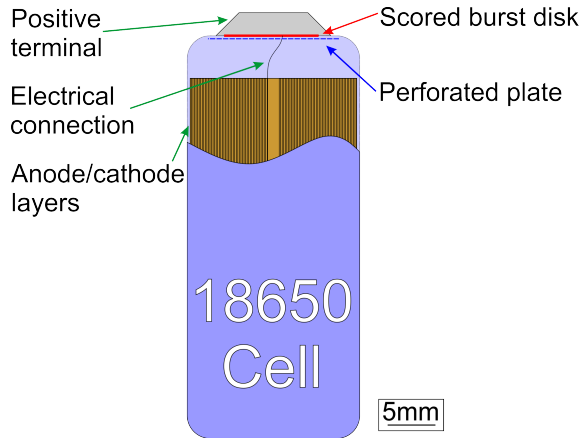
Figure 1.2: Schematic representation of the components in an 18650 format battery.

vent cap and the cathode. Once separated, vent caps were tested with the small crimped portion of the battery case still in place. Battery cases are constructed from very thin steel which did not interfere with the holding and sealing of vent caps in testing, as removing the remaining battery case from the vent caps would have risked damage to the vent mechanism itself.

Removal of vent caps from live cells requires delicate and precise work which is performed in collaboration with Sandia National Laboratories. Safety considerations include causing a thermal runaway event during the battery disassembly process, so all removals were performed by trained staff at Sandia. Of note, the process of intact vent cap removal was complementary to other research efforts. Removal of vent caps was already a step in battery disassembly process used to remove electrochemical components from cells and evaluate performance characteristics such as thermal stability [34].

1.4   Present research objectives

Novel experimental methods and test fixtures have been developed and applied here to characterize the venting process of 18650 format lithium ion batteries. Specifically, burst pressure, opening area, and discharge coefficient will be quantified. These parameters affect the external fluid dynamics and duration of a venting failure which are directly related to safety risks including flammability. Vent caps, independent from live batteries, will be tested to allow precise control of experiments with air rather than a volatile gas and liquid electrolyte spray.

Vent caps sourced commercially and removed from live 18650 format batteries will be tested and vent parameters are to be quantified. An extended test series of fifty commercially sourced vent caps will provide a baseline for understanding not only mean quantities but also the statistical distribution. Knowing

the distribution of vent cap flow parameters will provide additional understanding into the variability of abuse failures of live cells. Comparison between the commercially sourced vent caps and those removed from live cells will demonstrate the potential differences in venting failures. Last, the three main vent parameters will be compared on a vent-by-vent basis throughout the extended commercial vent cap test series to show any relations which may be present.

CHAPTER 2

VENT CAP BURST EXPERIMENT

2.1 Test fixture development

2.1.1 Burst measurement fixture design and fabrication

Due to the lack information on vent cap burst pressures in the literature and manufacturer specifications, tests were performed to measure this parameter. Under abuse testing or conditions, the internal pressure within the a lithium ion battery increases until the point where a pre-scored burst disk within the vent cap ruptures. To measure the pressure at which the onset of venting occurs, intact vent caps were burst by applying a source of regulated compressed air at steadily increasing pressure. Pressure was applied slowly to the caps without significant gas velocity for consistency between tests and comparability to actual abuse conditions.

A preliminary test fixture was constructed to roughly determine the burst pressure. Information from these trials was used to provide design constraints for the permanent burst measurement test figure. As shown in Figure 2.1, a vent cap was mounted securely within an aluminum block which is drilled and tapped to 1/4 NPT to accept a pressure transducer. This block was connected to a gas cylinder pressurized to 13.8 MPa. Multiple needle valves were used between the aluminum block and the gas cylinder to throttle the flow rate as low as possible. Each trial was performed by slightly opening the gas cylinder valve as data from the pressure transducer was recorded. The system was pressurized which led to the opening of the vent cap.

The initial burst pressure trials were performed on three vents removed from live LG HE2 batteries. Figure 2.2 shows the measured pressure traces of the three trials. The mean burst pressure was 1.92 MPa.

A permanent test fixture was constructed for direct pressurization of intact vent caps via a cylinder of compressed air. To achieve this, the holding mechanism seen in Figure 2.3 was designed and fabricated. The vent cap is held securely between a high pressure fitting and a hollow lock set screw. Laser cut silicone gaskets on either side of the vent cap seal the fixture. With the exception of the gaskets and an acrylic mounting plate, this design was entirely made made from off-the-shelf components.
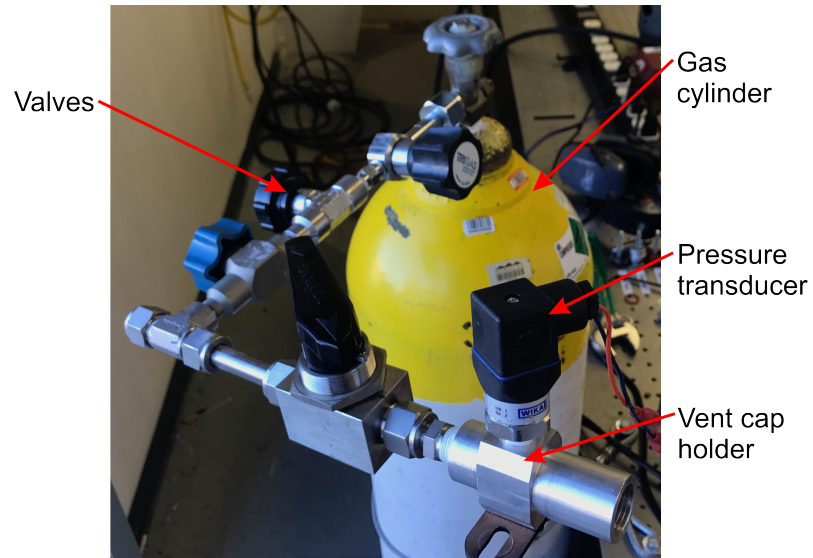
Figure 2.1: Test setup used to quickly perform initial burst pressure measurements with vent caps removed from LG HE2 batteries.
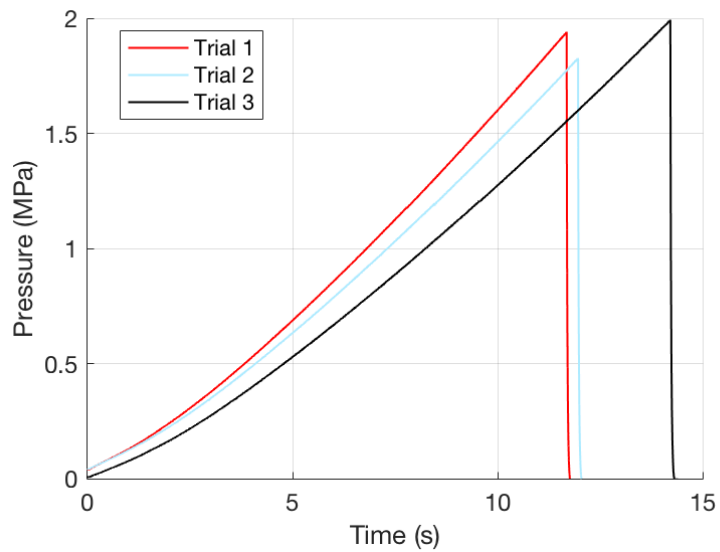
Figure 2.2: Pressure traces from initial burst pressure testing with LG HE2 vent caps.

A selection of brass and steel pipe fittings were used to construct the vent cap holding fixture rapidly without needing complicated machining. Air is supplied via a 12.7 mm outer diameter tube which is connected to the fixture with a stainless steel Swagelok tube fitting. The air supply was then directed through a ball valve to a main fixture body. This main structure was constructed from galvanized steel pipe nipples and Tees which allow for pressure measurement ports. The ball valve was used to stop the flow of compressed air once the vent cap has opened, thus ending the test. All pipe fittings used either tapered NPT threads or Swagelok style compression fittings, up to the main body of the fixture, after which straight threads were used to allow greater variability in vent cap thickness. A compact extreme pressure steel straight adapter was used to adapt from 3/8 NPT female to 7/8-14 UNF male threads. The minor diameter of 7/8-14 UNF threads is 20 mm which allows for sufficient clearance of the 18 mm diameter vent caps. A 7/8-14 UNF thread coupler was then used to surround the vent cap and align it with the silicone sealing gaskets. A hollow lock set screw was used to compress the gaskets and vent cap against the face of the extreme-pressure thread adapter. The 12.7 mm hexagon used for tightening the set screw allowed for an airflow channel once the vent cap bursts.

The vent cap holding fixture was mounted to an acrylic plate which is supported by four posts on an optical table located in the testing side of the laboratory. A length of high-pressure rated nylon tubing connects the vent cap holder to the compressed air supply which can be regulated between 0 MPa and 3.45 MPa. The pressure regulator was operated manually to increase pressure to failure during testing, and a dial type pressure gauge was used on the outlet of the regulator to confirm the reading from the pressure transducer installed on the vent cap holder. A follower hand on the downstream pressure gauge showed the maximum pressure in each test which will correspond to the vent burst pressure. A compressed air cylinder was used for vent testing as it could supply sufficiently high pressures. The gas cylinder and pressure regulator are shown in relation to the vent cap holder in Figure 2.4.

A second vent cap mounting apparatus has also been designed for incorporation of optical imaging techniques including high-speed schlieren and particle image velocimetry (PIV) for future testing. The design of this second fixture replaces the compact extreme pressure thread coupling with a brass 3/8 NPT to 1-8 UNC straight thread fitting, a custom holding ring, and custom compression nut. This assembly has been designed to securely hold provide sealing for a vent cap as shown in Figure 2.5 while maintaining a fairly unobstructed field of view adjacent to the vent openings. The only obstructions within the field of view are the two cantilevered teeth on the holding ring which keep the vent cap sealed against the silicone gasket. The front of the vent cap sits 0.5 mm past the front of the compression nut to ensure that the test apparatus is minimally obstructing the field of view. While testing has not been performed here, this design has been incorporated for future experimentation with the burst testing apparatus where optical techniques will be able to measure the flow fields of gases and particles as they are expelled through an opened vent. Tests on vent caps alone will provide a simple and repeatable baseline of experimental data to compare to future
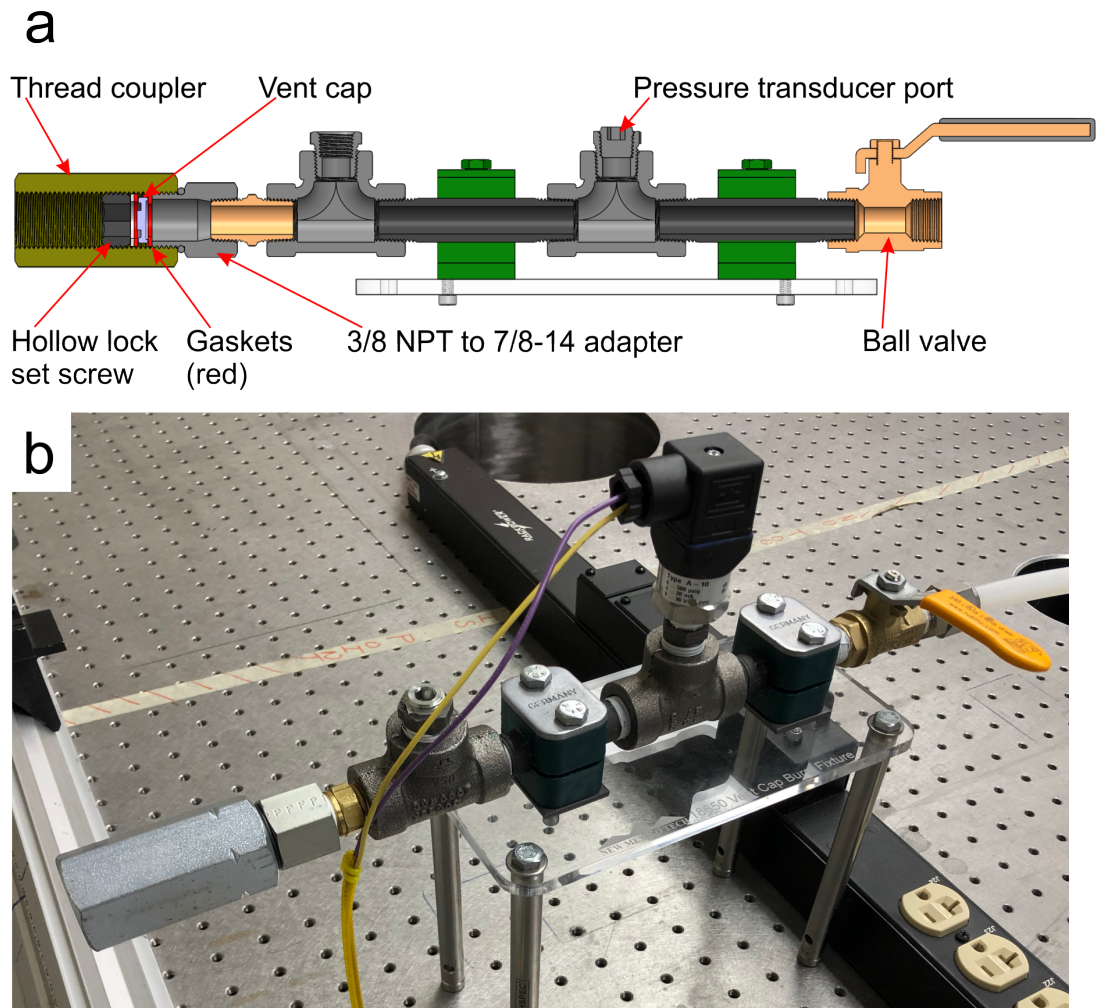
Figure 2.3: (a) An annotated cutaway view of the vent cap holding mechanism design, and (b) installed image of the fixture used for burst tests with various vent caps.
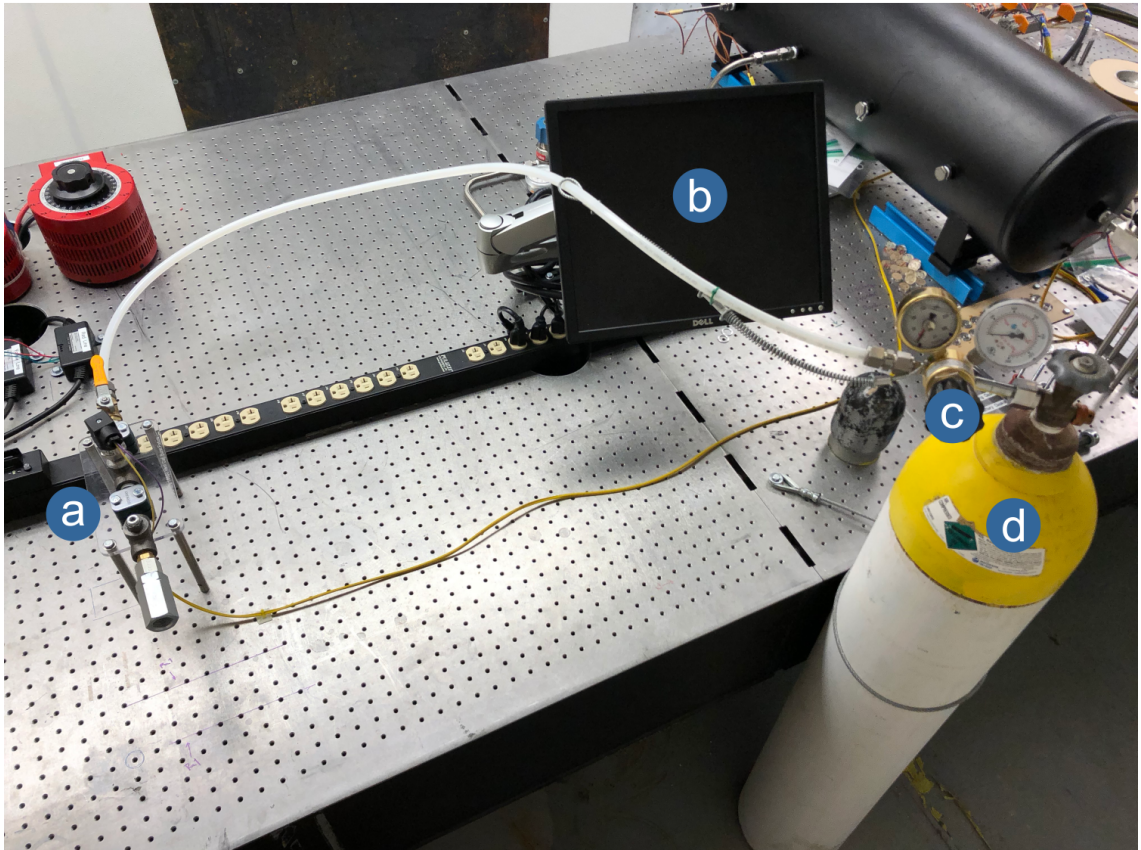
Figure 2.4: Overview of the laboratory setup with the (a) vent cap holder annotated, (b) computer screen used for pressure monitoring in LabVIEW, (c) pressure control regulator, and (d) gas cylinder.

imaging of liquids and gases vented during abuse testing.
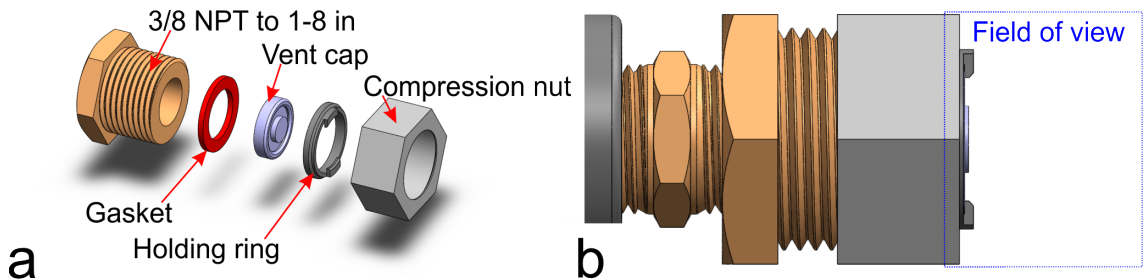
Figure 2.5: Model views of the modification to the burst pressure setup to allow visualization of venting flows including (a) an exploded view of the components and (b) the assembled setup with the planned field of view for optical diagnostics outlined in blue.

2.1.2 Data acquisition

All reported data was measured via a Wika model A10 pressure transducer with a measurement range of 0 MPa to 3.45 MPa to match the control range of the pressure regulator. The pressure transducer was powered with a fixed 12 V_{DC} supply, and the nominal 4 mA to 20 mA output was converted to a voltage signal by measuring the voltage drop across a 468.5 Ω resistor. This allowed the voltage measurements to be scaled linearly between 1.87 V and 9.37 V. Current-to-gage-pressure calibrations were provided by the manufacturer at 0.000 MPa, 1.724 MPa, and 3.447 MPa. A linear regression of these provided values was used in data processing.

Voltage was measured by a National Instruments 9205 card installed in an eight slot 9188 cDAQ chassis located on the optical table in the test side of the laboratory. This card was configured to measure analog voltages between -10 V and 10 V with 16-bit precision. Initiation of data acquisition and live monitoring of the pressure transducer reading was performed via a LabVIEW program run on a desktop computer and written specifically for the burst pressure testing. The desktop computer was located and operated in the control room of the laboratory which was separated from the testing side by a wall reinforced with steel sheeting. The pressure was measured at a rate of 1 kHz during all testing.

2.2 Procedure and sample data analysis

Prior to testing, system pressure was equalized with the atmosphere by fully decreasing the pressure control regulator output and opening the the ball

valve. The 7/8 in thread coupling was left installed by threading up to the O-ring on the extreme pressure 3/8 NPT to 7/8-14 UNF straight thread adapter. The battery vent cap was then installed within the thread coupling with silicone gaskets on either side. The aluminum washer was placed over the gasket on the outer side of the vent cap to prevent binding when the hollow lock set screw is then installed and tightened to light torque. The set screw was only tightened enough to provide even pressure between the vent cap and both gaskets. Proper alignment of all components was confirmed by applying light pressure with a steel awl to the positive terminal of the vent cap. If the vent cap was unable to move when pushed by the awl, then proper sealing had occurred. As the vent cap was installed with the system pressure at zero, all trials will begin at a gauge pressure of zero.

Individual tests were not started if the pressure in the compressed air cylinder is less than 3.45 MPa. As the gas cylinder sets the upper limit of pressure that can be applied to the vent cap in any given trial, it must have enough pressure to guarantee a burst or the system would have to be disassembled while components are pressurized.

Trials were begun by confirming a zero pressure reading and initiating data recording in LabVIEW by the test operator in the control room. The dial on the pressure control regulator was slowly and consistently turned manually by an operator in the test chamber to increase output pressure. A computer monitor in the testing side of the laboratory mirrored the screen seen by the operator in the control room so the operator opening the regulator can watch a real-time pressure plot. The operators watched the pressure as it climbed to ensure that no erratic or rapid pressure changes occur, so the test can be performed in a quasi-static manner. Pressure was increased manually until the vent cap opens. At this moment, the operator stopped adjusting the pressure regulator and immediately closed the ball valve to stop the flow of air. The other operator stops data recording and saves files accordingly.

After testing, data files were read into MATLAB where the measured pressure is plotted against time. Pressure data was smoothed via a moving average over a window of 20 ms. This smoothing reduced the noise band from a static measurement taken with the system open to atmosphere from a standard deviation of 1.132 kPa to 0.386 kPa. Figure 2.6 shows the smoothed pressure data from a commercially sourced vent cap distributed by Material Technology International Corporation (MTI). In this plot, annotations highlight the moments when: pressurization begins, the vent cap ruptures, the flow out of the system is momentarily choked, and the ball valve is closed to stop airflow. The steps in the pressure trace during the pressure rise period are due to the operator manually turning the dial on the pressure control regulator. As mentioned, the data has been smoothed with a moving average over a 20 ms window which is significantly shorter than these operational variations. Burst pressure was taken to be the maximum value within the smoothed dataset which was at 2.165 MPa in this trial. After the vent bursts, the pressure measurement immediately dropped, and the plateau before the airflow was stopped is due to the flow choking within

the system. The large pressure drop measured is consistent with airflow choking within the regulator. Thus, the plateau is characteristic of pressure regulator performance and did not provide any useful information.
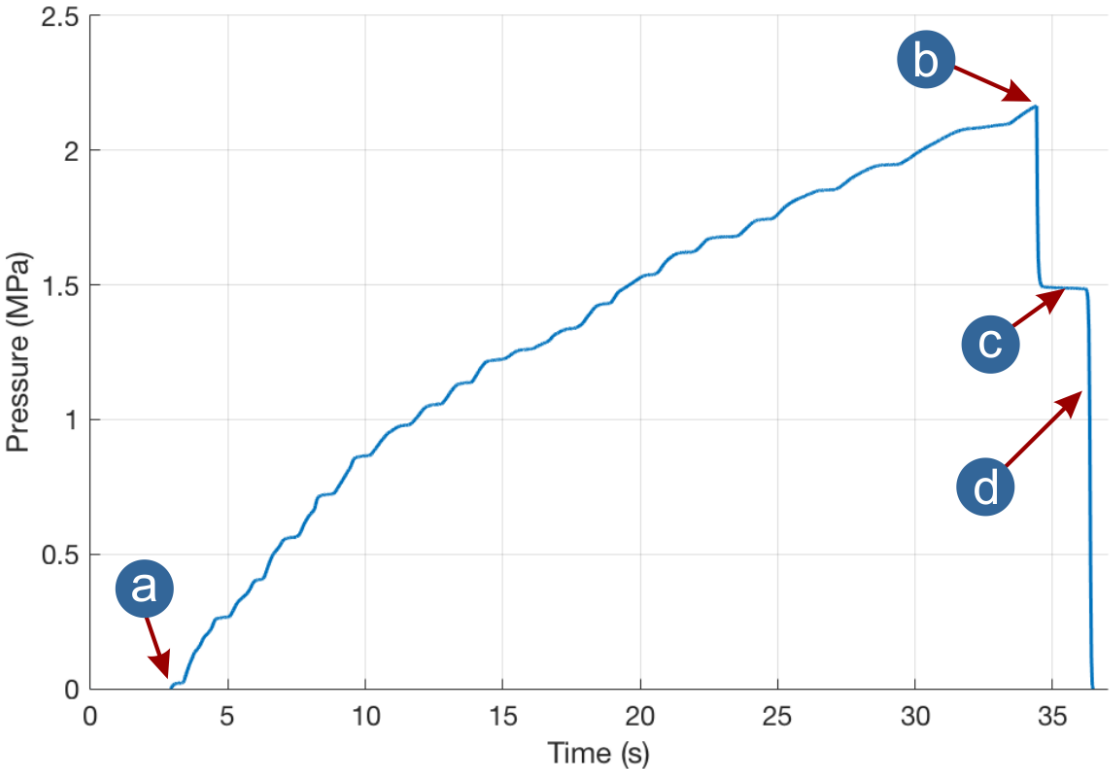
Figure 2.6: Annotated pressure trace taken from a MTI vent cap showing the (a) beginning of pressurization, (b) vent burst, (c) flow momentarily choking, and (d) the ball valve being closed by the operator to stop airflow and finish the experiment.

CHAPTER 3

CHOKED ORIFICE TESTING APPARATUS (COTA)

3.1   Design and fabrication of the COTA

3.1.1   System overview

Battery venting involves transient, pressure-, multi-phase driven fluid flow through an orifice into the atmosphere. This situation is complicated due to the intricate and unique geometry of the vent caps, multiphase flow of gaseous decomposition products and liquid electrolyte, and material properties accordingly difficult to quantify. Understanding the fluid flow leaving a battery during a failure event is important to quantifying how dangerous a venting event will be and how long it will last. Here the venting process experimentally modeled in a simplified scenario to allow for accurate and precise quantification of the vent's geometry and mass flow characteristics in terms of opening area and discharge coefficient respectively.

The COTA has been designed and fabricated to mimic the venting of gas through an 18650 size vent cap, but with simplifications made to allow for precise quantification of the flow. Specifically, this device uses dry air because the gas properties are well known compared to the multiphase mixture created within a lithium ion battery in an abuse situation. Also, the potential run time for testing has been increased by storing much more mass within the system which allows for larger datasets to be recorded. The vent caps used in tests with the COTA have been previously tested on the aforementioned burst pressure measurement test fixture. This is done because the vent caps will open and stay open during burst pressure testing.

Figure 3.1 shows annotated images of the COTA and it individual components. Major components included in this setup are the battery vent cap holder, an accumulator tank, pressure regulators, inlet and outlet valves, a compressed air cylinder, and instrumentation.

Air from the cylinder is used to pressurize the accumulator tank before testing. Testing with dry compressed air is necessary because initial testing with humid, compressed shop air resulted in freezing water vapor out of the air. The ice then deposited within sample orifices and battery vent caps and skewed results significantly. The first of two pressure regulators in series are used to reduce
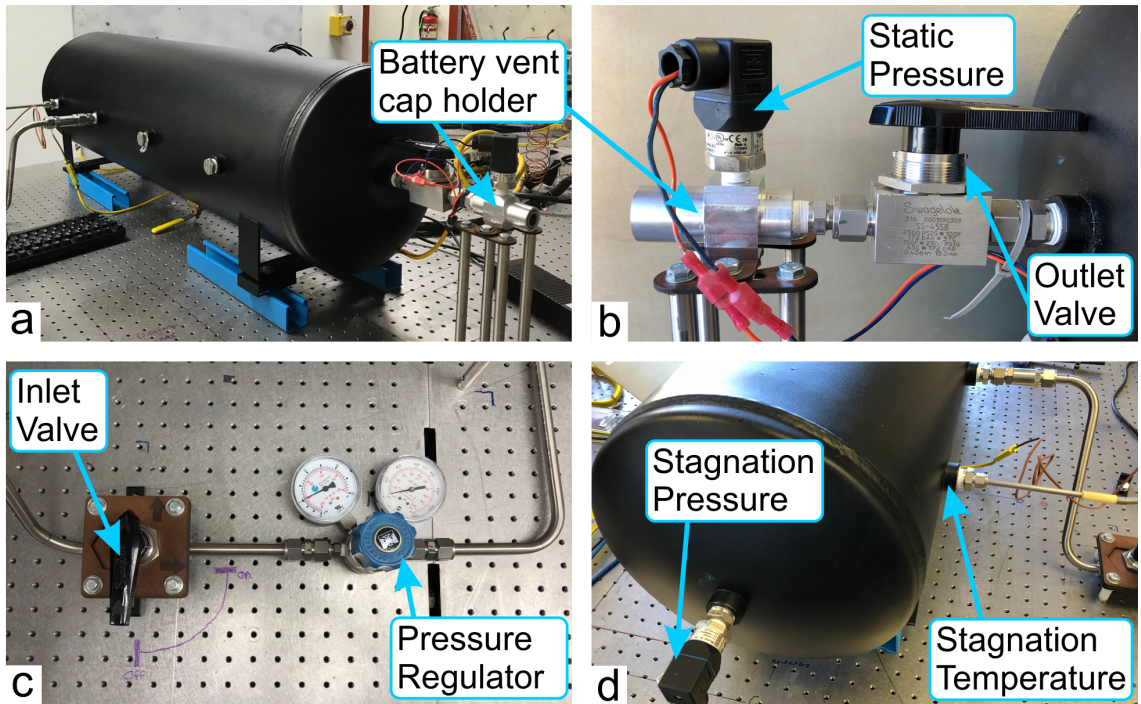
Figure 3.1: Annotated views of the COTA showing the (a) overall test setup, (b) battery vent cap holder with static pressure transducer and outlet valve, (c) the inlet valve and pressure regulator, and (d) the measurement locations of stagnation properties within the accumulator tank.

the pressure from the gas cylinder to a safe level to be used with the rubber tubing which connects the gas cylinder assembly to the accumulator tank assembly. Cylinder pressures as high as 13.8 MPa are lowered to a constant 690 kPa in the rubber tubing. The second pressure regulator further reduces pressure in the system to 276 kPa which is supplied through the inlet valve to the accumulator tank seen in Figure 3.1(a). The accumulator tank has a specified interior volume of 76 L and is rated to 1.03 MPa. The maximum pressure is not used because tests initiating from an initial tank pressure of 276 kPa generally maintains choked flow for between 10 s and 30 s depending on the size of the vent opening.

Since the vent caps and validation orifices are all open before being tested on the COTA, a Swagelok SS-45S8 ball valve (denoted the outlet valve in Figure 3.1(b)) is manually opened at the start of each test to initiate airflow. This ball valve was chosen because it is designed to maintain the inner diameter of the steel tubing connecting valve to the vent cap holder and to minimize pressure drop which could skew the results. Steel tubing used upstream of the vent cap holder has a cross sectional area of 94 mm^2 which is significantly larger than the potential opening area of vent caps tested here. Another Swagelok ball valve shown in Figure 3.1(c) is used on the inlet side of the accumulator tank to allow airflow into the system before testing and is closed once the desired 276 kPa is reached. Allowing no airflow into the tank during testing simplifies mass flow calculations to only out flow.

Stagnation pressure and temperature are both measured within the accumulator tank. As stagnation properties are achieved where gas velocity is zero, a pressure transducer is placed on the opposite side of the tank from the outlet as seen in Figure 3.1(d). This Wika model A10 pressure transducer has a measurement range of 0 kPa to 345 kPa. On the side of the tank near the stagnation measurement pressure transducer, an Omega K-type thermocouple probe with 6.35 mm outer diameter and an exposed junction is held in place with a Swagelok SS-400-1-8BT bored-through tube fitting using teflon ferrules.

3.1.2   Nozzle design of the battery vent cap holder

The battery vent cap holder within the COTA is designed to securely hold vent caps once removed from a battery and create an airtight seal with the upstream source of pressurized air. The vent cap holder can be seen installed in the test setup in Figure 3.1(a) and 3.1(b). A single vent cap is held firmly between two 7/8-14 UNF sized set screws, and silicone gaskets are used to create a seal. The set screws have a 12.7 mm interior hexagon which allows for fastening while leaving a central opening for unobstructed air flow out of the vents. This design allows for the battery cap to vary in height due to differences in manufacturing tolerance and removal procedure. The cap holder can accept caps up to 20.6 mm in diameter. A short length of tubing connects the battery cap fixture to the outlet valve and accumulator tank.

The main body of the vent cap holder is machined from a single piece of 38.1 mm hexagonal aluminum stock. To ensure concentricity of all internal features, the stock was turned down to 28.58 mm on both ends to be able to fit into a lathe collet. As these two exterior profiles were cut without re-fixturing, they are concentric to each other. This allows the part to be machined from either end precisely which is critical when cutting the necessary threads and tapers Between different sections of the vent cap holder, tapers are included to streamline the flow. Tapers are all made with the tip of a 12.7 mm twist drill with a 118° chisel point, so flow undergoes a 59° turn along the interior walls of the holder. Additional machining was performed to add 8-32 UNC blind tapped holes for securely mounting the vent cap holder in optical rods.

The center of the battery holder is machined to a precisely known cross-sectional area. A small sensing orifice with a diameter of 1.4 mm allows for measurement of static pressure throughout testing which is used in calculations to determine the opening area of each vent cap. The sensing orifice leads to a Wika model A10 pressure transducer which is mounted directly into the body of the vent cap holder. The cross sectional area at the sensing orifice of 40.0 mm^2 is chosen to be larger than the maximum possible opening area of a battery vent cap, based on a survey of the perforated plates on the internal side of vent caps from cells of interest. The 40.0 mm^2 cross section was cut with a K size drill bit. Additionally, the same care has been taken when selecting all fittings with sufficiently large cross sectional areas between the accumulator tank and vent cap. This ensures that when venting flow will choke at the vent cap rather than anywhere else within the system.

The internal flow between the accumulator tank and vent cap can be calculated as an isentropic, one dimensional nozzle as shown in Figure 3.2. The cross section decreases as the as flow is accelerated from the tank to the exit plane at the opening of the battery vent cap, and sudden changes are minimized by allowing tapered transitions between different sections of the holder. By designing the vent cap holder as a converging nozzle with the vent opening at the exit plane, opening area can be calculated when the physical state of the air and geometry of the flow channel are known at another point within the nozzle.

3.1.3 Measurements and data acquisition

Temperature and pressure are recorded and monitored simultaneously with a National Instruments cDAQ data acquisition system controlled by LabVIEW program written for this specific test. Similar to the burst pressure measurement testing, a 12 V$_{DC}$ power supply is used to power both 0 kPa to 345 kPa pressure transducers. Again, the 4 mA to 20 mA current output is converted to a voltage measurement within the range of the NI 9205 analog card by measuring the voltage drop over a nominally 470 Ω resistor. Temperature is measured directly by a NI 9212 card with internal cold junction compensation, and the thermocouple lines have been shielded to minimize signal noise caused by

Vent Cap Holder: **1-D Nozzle:**

7/8-14 tapped

Battery cap

Hollow-lock set
screws (black)

Sealing gaskets
(red)

Tapped for pressure
transducer

1.4 mm orifice

3/8 NPT tapped

Measure: P_{atm}

Calculate: A_e

Measure: P_1
Known: A_1

Measure:
P_0 and T_0
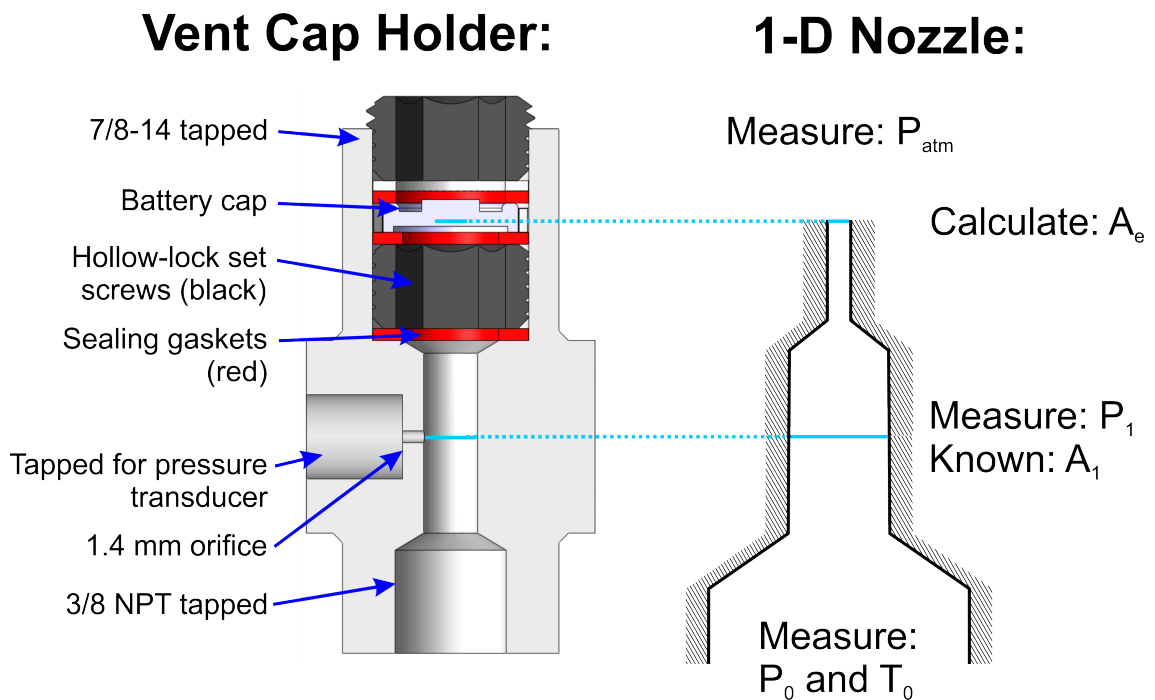
Figure 3.2: An annotated cutaway model of the vent cap holder compared to a schematic representation of the vent cap holder as a one dimensional nozzle with varying cross section. Horizontal blue lines show the relative locations of the vent cap and static pressure measurement between the model and schematic.
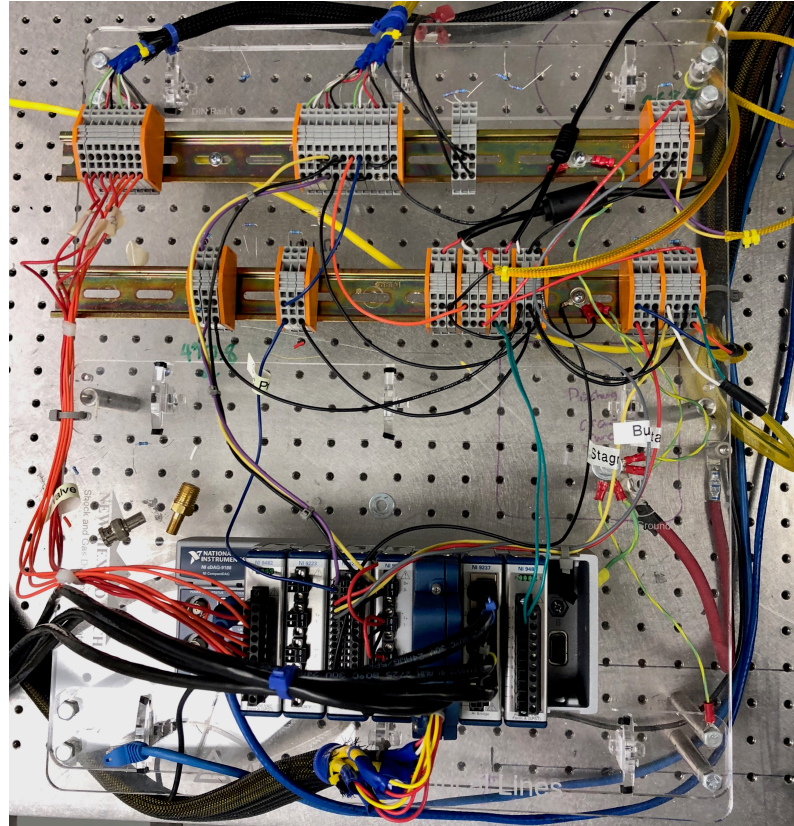
Figure 3.3: The National Instruments cDAQ 9188 installed in the test side of the laboratory which is used for COTA and burst pressure measurement experiments.

nearby equipment. Figure 3.3 shows how the data acquisition system is installed on the optical table in the testing side of the laboratory on a laser cut acrylic sheet. Nearby DIN rails with Wago brand connectors are used for direct current power distribution, construction of the small current to voltage measurement circuits, and strain relief. Data acquisition rates for the temperature and pressure measurements are 100 Hz and 1 kHz, respectively.

Manufacturer calibrations are used for temperature and pressure measurements. The National Instruments thermocouple card uses the initial manufacturer calibration. Individual thermocouple calibration is not performed, but an additional exposed junction, K-type thermocouple probe is used to measure room temperature throughout testing and is confirmed against an Extech SD700 portable weather station. Wika A10 pressure transducers are provided with factory calibration results with 7 Pa precision, and linearity is confirmed. A linear fit to this calibration data is used to calculate gauge pressure from the transducer's output current. The resistance of the nominal 470 Ω resistors used to convert between current output and an analog voltage measurement are mea-

sured with a Fluke 115 multimeter to 0.1 Ω resolution. Additionally, analog dial pressure gauges are installed on the COTA for test operator confirmation that measurements appear accurate during testing. Utilizing factory calibrations allows a degree of confidence in measurement accuracy. Periodic reconfirmation of instrumentation calibration is necessary to avoid measurement bias. Pressure transducer calibration can be the most influential source of measurement bias as these measurements have the largest relative variation within individual trials.

3.2 Venting parameter calculation methodologies

3.2.1 Opening area

The opening area of the vent cap is inferred via the measured relationship between static and stagnation pressures. Within the test setup, three distinct locations are considered in the analysis: stagnation within the tank, the known cross-section in the vent cap holder, and the opening in the battery vent itself with subscripts 0, 1, and e, respectively.

Once the vent opens and allows air to leave the system, the static pressure measurement taken in the vent cap holder (P_1) will be lower than the stagnation pressure (P_0) at any given instant. Making the assumptions that the flow within the system is isentropic and the air behaves as an ideal gas, the Mach number (M_1) of the flow through the vent cap holder can be calculated via the isentropic flow relation in Equation 3.1 where γ is the ratio of constant pressure to constant volume specific heats for the air [35, 36]:

$$\frac{P_0}{P_1} = \left(1 + \frac{\gamma - 1}{2} M_1^2\right)^{\frac{\gamma}{\gamma-1}} \tag{3.1}$$

Once the calculation of Mach number through the vent cap holder is complete, it can be used along with the known cross-sectional area at this location (A_1) and Equation 3.2 to calculate the area at which the flow is choked (A^*), which is the vent area:

$$\frac{A_1}{A^*} = \frac{1}{M_1} \left(\frac{\frac{\gamma+1}{2}}{1 + \frac{\gamma-1}{2} M_1^2}\right)^{\frac{\gamma+1}{2-2\gamma}} \tag{3.2}$$

By inspection of the one dimensional nozzle approximation of the battery vent cap holder, the sonic location ($A*$) is clearly the opening area (A_e). Equation 3.2 can be used to more rigorously demonstrate this by substituting $M_e = 1$. The right hand side of the area ratio equation is reduced to unity which demonstrates that $A_e = A*$ when the flow is choked.

In all tests, the pressure is initially enough to create a choked flow condition. For this to occur, the absolute pressure to open the vent must be 1.89 times atmospheric pressure or greater [35]. As this pressure differential creates a choked flow, it is known that the Mach number of air passing through the vent cap will be fixed at unity until the stagnation pressure drops below 76 kPa gauge (using a value of 86 kPa for atmospheric pressure as measured in the laboratory). If the flow is no longer choked at the vent opening, Equations 3.1 and 3.2 can still be used with the additional assumption that the flow exits the system through the vent cap with static pressure equal to atmospheric pressure. Accordingly, Mach numbers can be calculated at the vent cap holder (M_1) and vent cap (M_2). Equation 3.2 provides area ratios A_2/A^* and A_1/A^* at these two locations. Letting A^* become an arbitrary location for the sonic condition, the vent cap opening area (A_2) can be calculated in terms of the known value for A_1.

Comparing the isentropic flow equations for pressure and area ratios can also aid in the test fixture design when attempting to measure opening area via static and stagnation pressure measurements. Specifically, A_1 can be optimized for the range of anticipated orifice areas. Figure 3.4 shows the ratio of static pressure to stagnation pressure (P_1/P_0) versus the opening area normalized by the known area (A^*/A_1). The plot was made by solving Equations 3.1 and 3.2 with Mach numbers varying from zero and one. In the plot, the trend demonstrates that the measurable difference between static and stagnation pressures is largest as the opening area approaches the size of the known cross section. Conversely, distinguishing between signal and noise in pressure ratio measurements when the opening area is an order of magnitude smaller than the known cross section becomes difficult.

3.2.2 Discharge coefficient

The discharge coefficient describes how efficient mass flow through a given obstruction is when compared to the maximum possible mass flow rate. The need for this parameter arises as analytical calculations often ignore viscous losses and turbulence for simplicity, but these effects become significant when flow is concentrated through a relatively small orifice of other form of obstruction. Discharge coefficient simply defined as the ratio between actual ($\dot{m}_a$) and theoretical mass flow ($\dot{m}_t$) rates as shown in Equation 3.3:

$$C_d = \frac{\dot{m}_a}{\dot{m}_t} \tag{3.3}$$

While discharge coefficient calculation is generally simplified and related to pressure drop across an obstruction within a piping system, the COTA vents directly to atmosphere and does not have any measurement capability downstream of the vent cap. The relation used for theoretical mass flow rate comes directly from the isentropic flow relations. Mach number is taken to be unity as
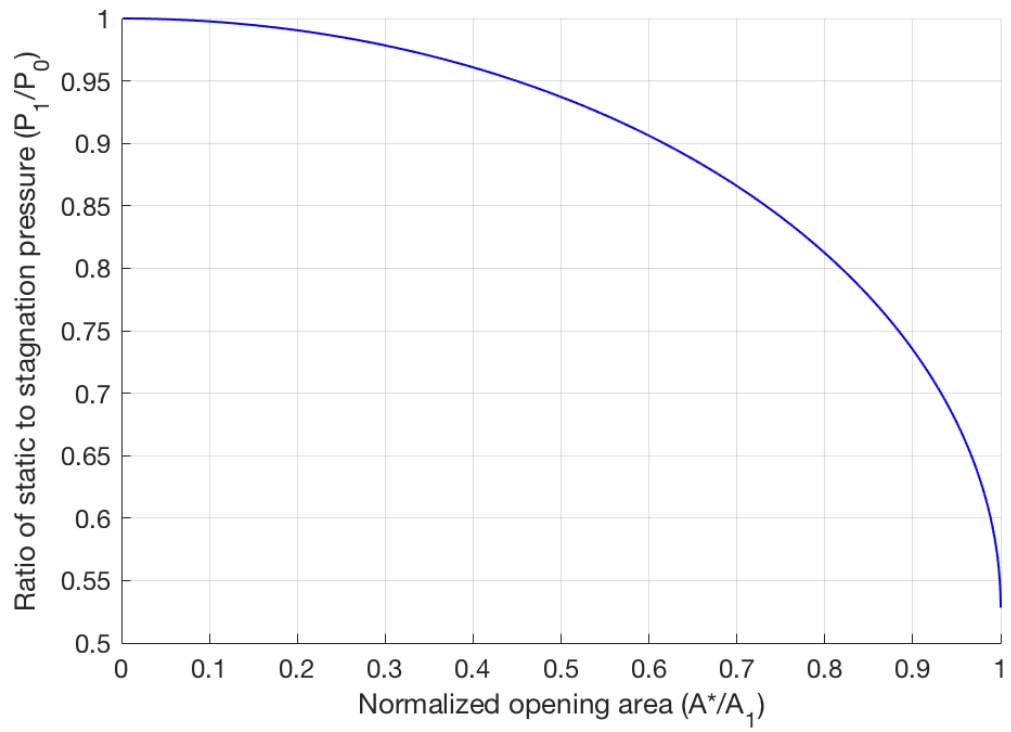
Figure 3.4: Comparing the ratio of pressure measurements to normalized opening area in a choked flow scenario.

calculations are made only when the flow is choked within the vent cap. The basic equation $\dot{m} = \rho A v$ is rewritten for compressible flow in terms of stagnation properties and Mach number as shown in Equation 3.4:

$$\dot{m}_t = \frac{P_0}{\sqrt{RT_0}} A \sqrt{\gamma} M \left(1 + \frac{\gamma - 1}{2} M^2 \right)^{\frac{\gamma+1}{2-2\gamma}} \tag{3.4}$$

Equation 3.4 is simplified for evaluation at the vent cap opening where the flow is choked to Equation 3.5 by substituting a Mach number of one and the cross sectional area (A^*).

$$\dot{m}_t = \frac{P_0}{\sqrt{RT_0}} A^* \sqrt{\gamma} \left(1 + \frac{\gamma - 1}{2} \right)^{\frac{\gamma+1}{2-2\gamma}} \tag{3.5}$$

A commercial flow meter would be the ideal means of measuring the actual mass flow rate out of the COTA in terms of accuracy as the equipment would be calibrated and well characterized. However this method becomes impractical due to the large flow rates seen in testing which would require highly specialized and costly flow meters. Instead, mass flow rate is approximated from conservation of mass for an Ideal Gas as shown in Equation 3.6 for the venting process:

$$\dot{m}_a = -\frac{V}{R} \cdot \frac{d}{dt} \left(\frac{P_0}{T_0} \right) \tag{3.6}$$

This method allows for a simple approximation of the actual mass flow rate from the system with the known tank volume and gas constant along with the already measured stagnation temperature and pressure.

3.3 Testing procedure and example dataset

Prior to testing, the accumulator tank is drained and relieved of any potential pressure from room temperature fluctuations by opening a ball valve located on the bottom of the tank. The battery vent cap is then installed between two silicone gaskets. An aluminum washer is then also placed in the 7/8-14 UNF section of the vent cap holder before a hollow lock set screw is installed with a hexagonal L-wrench. Specific care is taken to not over torque the set screw as bulging of the gaskets could potentially block some of the openings on the perforated plate within the vent cap. These parts are all visible in the cutaway model of the vent cap holder in Figure 3.2. Of note, the upstream hollow lock set screw is not removed between testing as its only purpose is to provide preload to the first silicone gasket.

After the vent cap is installed within its holder, the LabVIEW program for COTA testing is run continuously so pressure within the tank can be monitored

by the real-time stagnation pressure readout. The second regulator in the series is adjusted to an output of 276 kPa. Pressurization of the accumulator tank is done by first closing the outlet valve and then opening the inlet valve. The inlet valve is closed once the tank has been fully pressurized to 276 kPa. The test operator monitoring the LabVIEW program in the control room then initializes data recording. Once the test operator has confirmed that the data output files are being continually written and saved to the computer's hard disk, the test operator in the room is instructed to open the outlet valve. Static and stagnation pressures are carefully observed to notice any irregularities in the test. Data recording is stopped once stagnation pressure reaches 6.8 kPa as a sufficiently large dataset has already been collected when compared to the long amount of time for this final amount of tank pressure to equalize with atmosphere.

Of note, both test operators are required to wear both hearing and eye protection throughout the testing procedure. The sound level of the airflow exiting the COTA has not been quantified, but qualitative observation suggests that it would be unsafe for unprotected hearing. While no breakup of the vent caps leading to small projectiles is anticipated, personal protection equipment is still required.

After recording the data with the National Instruments system, the LabVIEW *.lvm* data files are converted to plain *.txt* format and are read into MATLAB. Since the thermocouples and pressure transducers are run at different sampling rates (100 Hz and 1 kHz respectively), two data files corresponding to the two sensor types are recorded with each test. Figure 3.5 shows a sample dataset from validation testing with a mock MTI vent cap. Stagnation pressure is initially at 276 kPa and drops immediately when the outlet valve is opened while static pressure jumps up to the appropriate value for the given opening area. Of note, the ratio of the absolute static pressure to stagnation pressure (P_1/P_0) is constant while stagnation pressure is above 76 kPa as is expected because the flow is choked.

3.4   Experimental validation with known orifices

3.4.1   Laser cut acrylic orifices of known size and various geometries

A series of orifice plates were fabricated for validation of the opening area calculation methodology. These plates were installed and tested as direct substitutes for the battery vent cap in the COTA. Twenty circular orifices shown in Figure 3.6 and ranging in area from 3.16 mm^2 to 37.4 mm^2 were tested. Each circular validation orifice is sized to correspond with a number or letter gauge drill bit. The initial profile of each orifice was laser cut with a Universal Laser Systems ULS6.60 with a slightly undersized inner hole. The laser cutter was also used to etch the drill size into each orifice plate. The circular orifices were then drilled
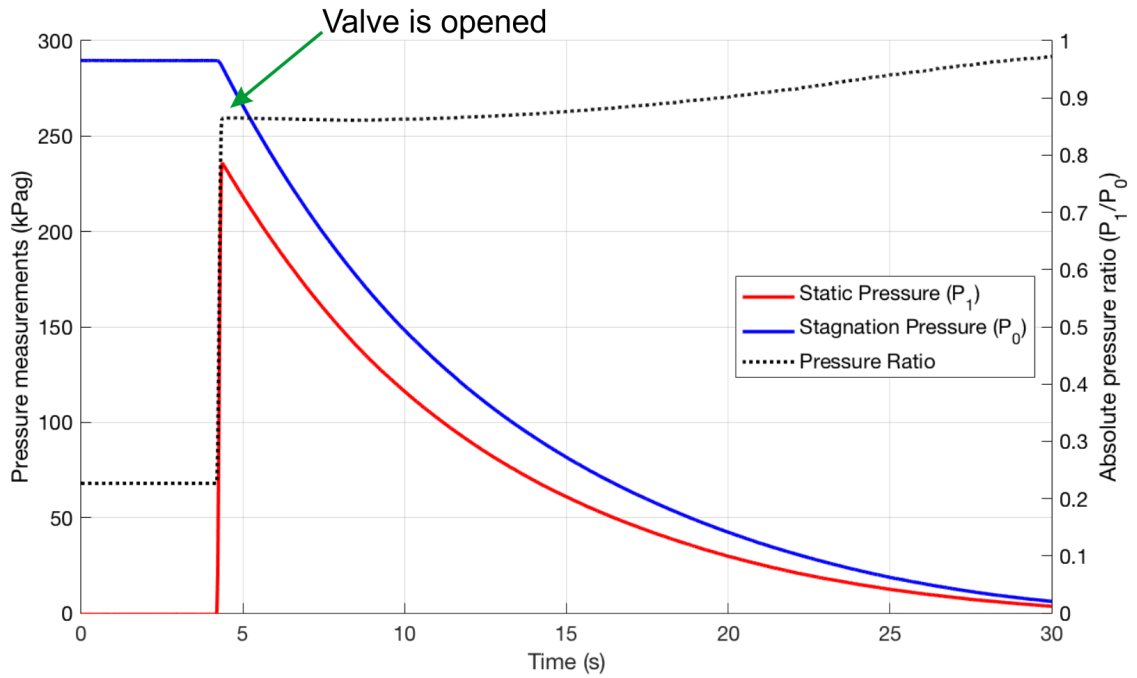
Figure 3.5: Example dataset from validation testing on the COTA with a mock MTI orifice.

Figure 3.6: Circular orifice plates made for validation of opening area measurements placed in a laser cut wood organizer.

using the prescribed drill bit size and chamfered. Dimensions of the holes were confirmed by measurements with digital calipers.

Additionally, four mock vent orifices seen in Figure 3.7 were created representing the intricate geometry and maximum opening area of vent caps removed from live cells manufactured by LG, Panasonic, and A123 along with the commercially sourced MTI cap. This was done by mimicking the cutouts in the perforated plate on the interior side of the vent cap. While it was unknown if the cross section would become smaller within the vent mechanism, the perforated plate is a clear upper limit to the opening area. The perforated plates were modeled in SolidWorks and imported into CorelDRAW X7 for labeling and laser cutting.
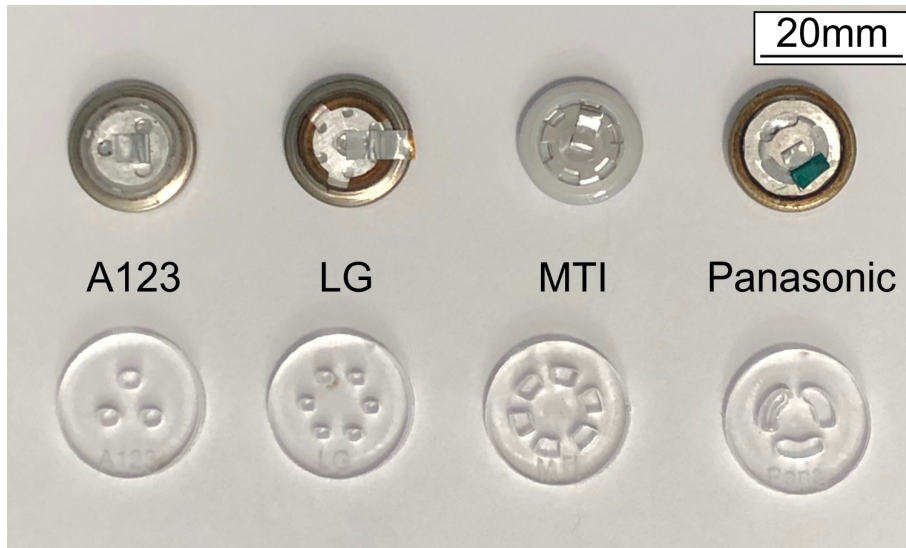
Figure 3.7: The internal surface of battery vent caps from 18650 format cells made by LG, Panasonic, A123, and MTI and orifice plates made to mimic the maximum possible opening area.

Individual trials performed on each of the circular orifices show strong agreement between actual and experimentally calculated opening areas throughout the range of possible vent cap opening areas. The results of this validation series are presented in Figure 3.8. The orifices designed to resemble the battery vent caps in Figure 3.7 show similarly accurate agreement between the actual and calculated opening area. Calculated opening area values for all acrylic orifices are tabulated in Appendix B.1.

Additionally, three of the twenty circular orifices were chosen for repeated trials to confirm the consistency of the system. The three orifices have areas of 18.5 mm^2, 27.7 mm^2, and 34.5 mm^2 which correspond to standard drill sizes of 11, A, and G respectively. Each orifice was tested five times, and the measured ratio between static and stagnation pressures was used to calculate the opening area. The results of these tests shown in Table 3.1 demonstrate the accuracy and repeatability of this experiment.

27
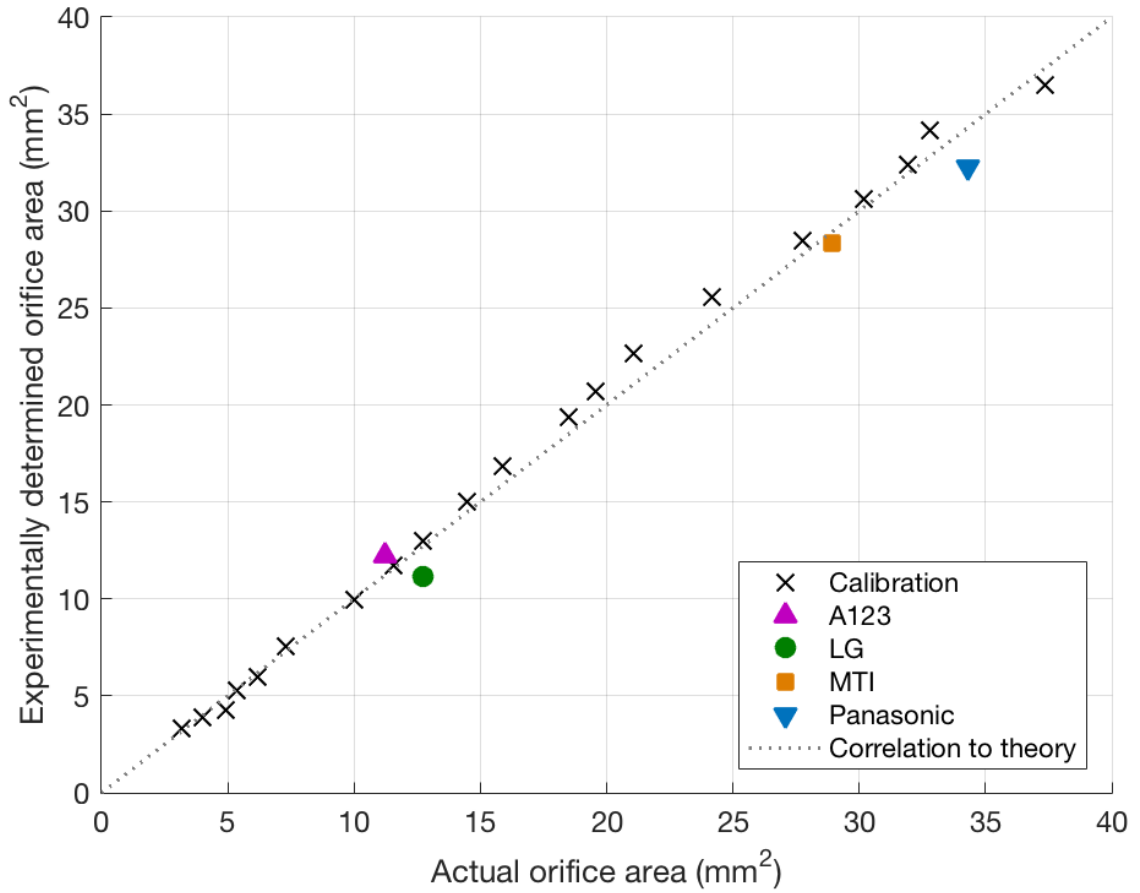
Figure 3.8: Comparison between actual and calculated opening areas from the validation series performed on the COTA. Orifices with circular and more complex geometries can be measured accurately with this experiment and calculation methodology. Experimentally determined opening areas had an uncertainty smaller than the symbol size on the plot.

Table 3.1: Opening area results from repeated trials

Test	Actual area (mm^2)	Calculated area (mm^2)
11 Drill, Run 1	18.5	19.4
11 Drill, Run 2	18.5	19.5
11 Drill, Run 3	18.5	19.5
11 Drill, Run 4	18.5	19.6
11 Drill, Run 5	18.5	19.7
A Drill, Run 1	27.7	28.2
A Drill, Run 2	27.7	28.3
A Drill, Run 3	27.7	28.3
A Drill, Run 4	27.7	28.4
A Drill, Run 5	27.7	28.4
G Drill, Run 1	34.5	34.4
G Drill, Run 2	34.5	34.4
G Drill, Run 3	34.5	34.4
G Drill, Run 4	34.5	34.4
G Drill, Run 5	34.5	34.4

3.4.2 Recreating and testing orifices described in literature

Test orifices were fabricated to match some of the experiments by Kayser who reported extensive experimental results including discharge coefficient in choked flow conditions [37]. Seen in Figure 3.9, the straight bore "S1" and "S2" orifices were turned from aluminum stock. The S1 and S2 orifices have interior diameters of 1.13 mm and 1.41 mm respectively, and both orifices have a thickness of 3.17 mm. The outer diameter is turned to 20 mm to closely fit into the COTA similar to the acrylic orifice plates. The holes drilled to make the orifices are left with sharp edges without a chamfered or rounded edge.

Discharge coefficient was calculated throughout the choked duration of the test and compared to the data reported by Kayser [37]. Discharge coefficient is plotted against the stagnation pressure normalized by atmospheric pressure, and the datasets are compared in Figure 3.10. This testing demonstrates that the discharge coefficient measurements with the COTA contain similar trends to previous experiments. Specifically, discharge coefficient is constant when P_0/P_{atm} is between 2.25 and 3.50, discharge coefficient increases with opening area, and the values measured with the COTA have similar magnitude to Kayser.
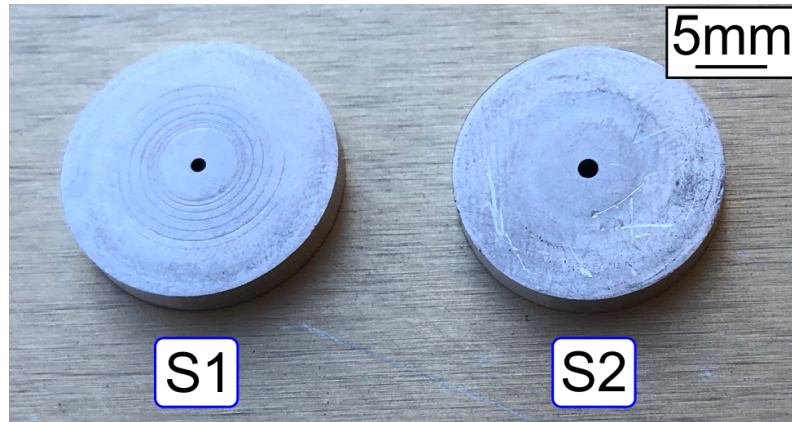
Figure 3.9: S1 and S2 orifice disks machined for comparison with Kayser, 1990.
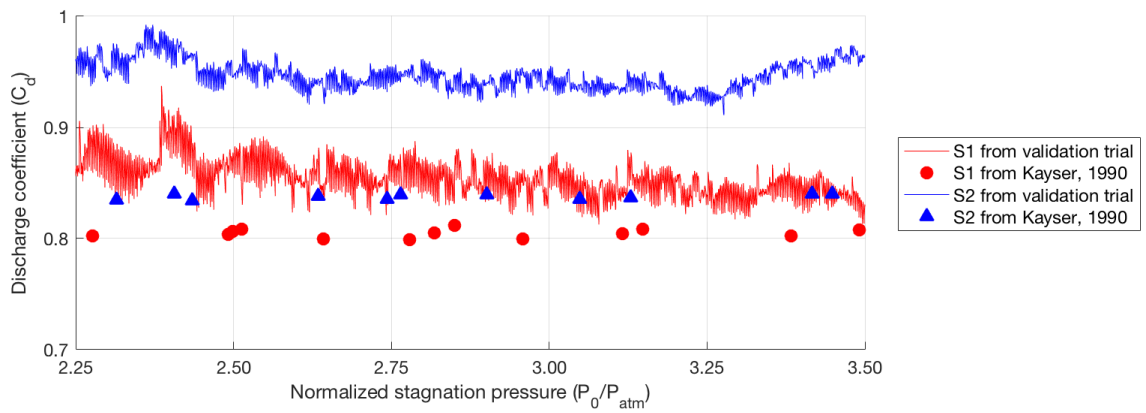
Figure 3.10: Discharge coefficient versus normalized stagnation pressure for testing with S1 and S2 orifices.

CHAPTER 4

EXPERIMENTAL RESULTS AND DATA ANALYSIS

4.1 Burst pressure measurements

4.1.1 Statistical distribution

A main test series of 50 commercially sourced vent caps from MTI and another set of four vents removed from live LG HE2 batteries were tested for burst pressure, opening area, and discharge coefficient. The size of the MTI test series allows for evaluation of the statistical distribution of vent cap burst and venting parameters. LG tests have not been exhaustively performed due to the complexities of the disassembly of live batteries. It is anticipated that the broad statistical characteristics of vent cap performance and trends between parameters will be consistent between manufacturers. This assumption is made because vent caps from all manufacturers follow the same general construction method with a thin, scored burst disk between a perforated plate and battery electrical terminal. However, the tests with LG vent caps are presented to provide context as to potential differences in mean values for burst pressure, opening area, and discharge coefficient.

After performing the fifty MTI tests, statistical properties were calculated and a reported in Table 4.1. The entirety of the raw data is present in Appendix B.2.1. Additionally, a histogram of the data is shown in Figure 4.1. Binning was automatically calculated within MATLAB according to Scott's rule which is optimized for data which appears similar to the Normal distribution [38]. These even bin widths of 0.1 MPa between 1.9 MPa and 2.4 MPa show how the data is relatively symmetric about the central bin which contains the mean of the dataset. Additionally, the minimum and maximum values for burst pressure are roughly the same distance from the mean.

Since the burst pressure data has a Normal distribution, an number of expected occurrences was calculated for each of the bins. While the counts of experimental occurrences in each bin must have an integer value, the expected occurrences is calculated numerically in MATLAB with the Normal Probability Density Function (PDF) tool. The Normal PDF was integrated with the data's mean and standard deviation between the boundaries of each bin and then scaled by the fifty tests ran. Table 4.2 shows how the experimental data is comparable to the Normal distribution.

Table 4.1: Statistical properties of burst pressures

	MTI	LG
Mean	2.158 MPa	1.906 MPa
Minimum	1.971 MPa	1.829 MPa
Maximum	2.364 MPa	1.961 MPa
Standard deviation	0.081 MPa	0.060 MPa
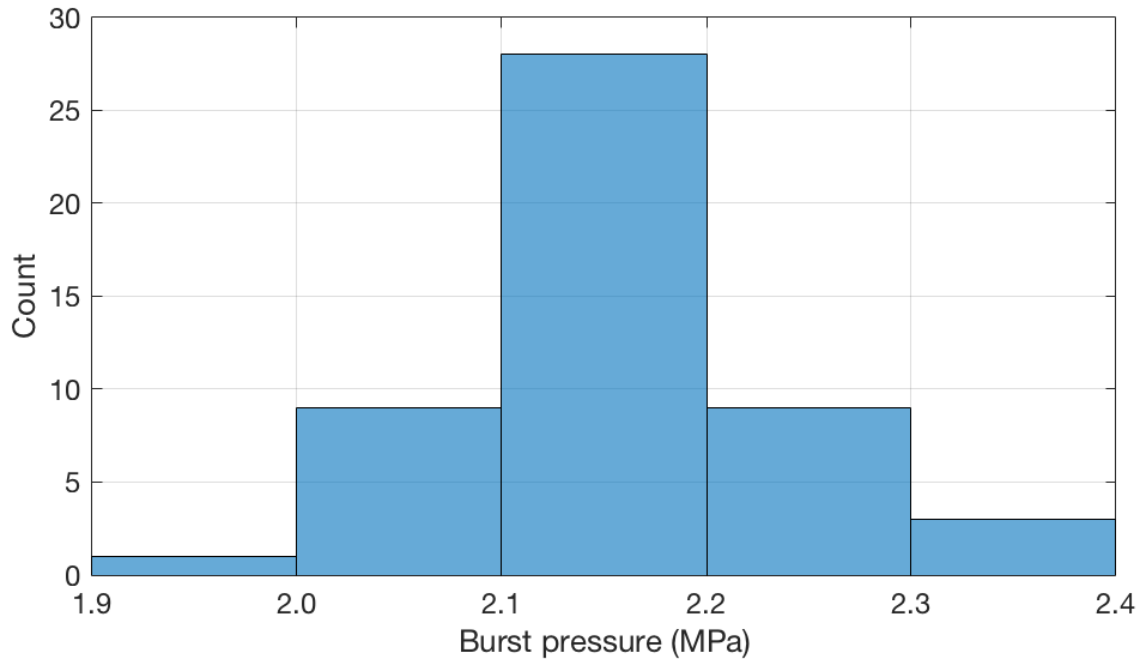
Figure 4.1: Histogram of MTI burst pressure data

Table 4.2: Comparing MTI burst pressures to the Normal distribution

Bin range (MPa)	Experimental occurrences	Expected occurrences
1.9 to 2.0	1	1.230
2.0 to 2.1	9	10.53
2.1 to 2.2	28	23.05
2.2 to 2.3	9	13.15
2.3 to 2.4	3	1.928
Total	50	49.89

The LG tests had burst pressure statistics listed in Table 4.1. The raw data from the four tests is shown in Appendix B.2.2. This limited trial set has significantly lower burst pressures than the MTI caps. Of note, all LG burst pressures are lower than the minimum burst pressure from the MTI series.

4.1.2   Complete and partial detachment of burst disks

It was observed that after some of the trials, the burst disk would become entirely detached within the vent cap. In all cases, the positive electrical terminal of the battery blocks the burst disk from being launched from the test apparatus as a projectile. Specifically, 15 of the 50, or 30%, of the MTI vent caps showed complete disk detachment while no LG cell had a full detachment. Reported in Table 4.3, the tests with detached and attached burst disks have similar mean and maximum values. However, the detached disks show a smaller standard deviation and the minimum measured burst pressure is much higher than the attached disks. For detached burst disks, the mean pressure was much closer to the minimum than the maximum. The attached burst disks had a mean close to the average of the minimum and maximum values.

Table 4.3: Statistical properties of MTI vent caps attached and detached burst disks

	Attached disk (MPa)	Detached disk (MPa)
Mean	2.150	2.177
Minimum	1.971	2.104
Maximum	2.340	2.364
Standard deviation	0.087	0.064

Once segregated into vent caps with burst disks remaining attached or becoming detached after testing, Figure 4.2 shows two trends. Binning is retained from Figure 4.1. The attached vent caps remained close to the Normal distribution. The detached burst disks showed a relatively high minimum value and the number of occurrences decreasing with increasing burst pressure. These distributions are also tabulated in Table 4.4.

4.1.3   Audible failure of electrical connection within vent cap

In testing both the MTI and the LG vent caps, an audible response from the vent cap was noticed at approximately 1 MPa. The sound was sufficiently loud to be heard while wearing hearing protection, and both test operators described it as a "tick" or a small "pop." This event was unable to be resolved because fluctuations in the pressure versus time data were present due to the test operator manually increasing the pressure regulator setting.
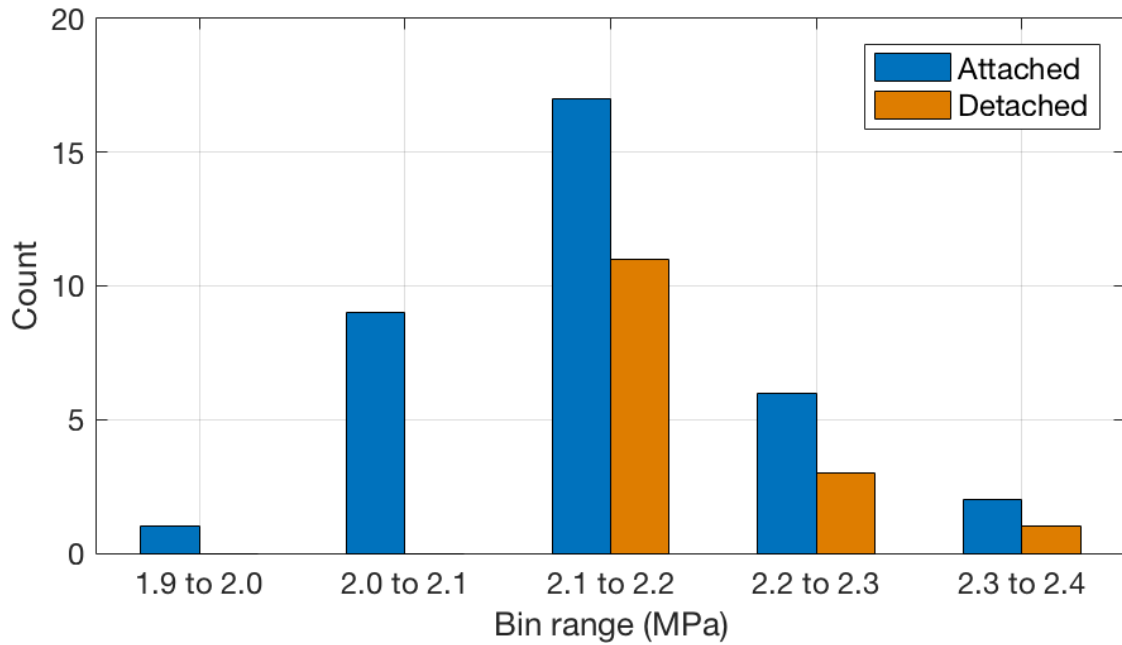
Figure 4.2: Histogram of MTI burst pressures from vent caps with attached and detached disks

Table 4.4: Data from Figure 4.2

Bin range (MPa)	Attached disk count	Detached disk count
1.9 to 2.0	1	0
2.0 to 2.1	9	0
2.1 to 2.2	17	11
2.2 to 2.3	6	3
2.3 to 2.4	2	1
Total	35	15

Another test was performed with an MTI vent cap where pressure was increased as normal, but when the audible response from the vent cap was heard, the pressure regulator setting was immediately held constant. The ball valve on the burst pressure measurement fixture was then closed, and pressure was released by manually removing a 1/4 NPT set screw from one of the steel Tee fittings on the device. Pressure recorded during this experiment is shown in Figure 4.3(a). Since pressure was no longer increased after the audible response from the vent cap, a small instantaneous drop in pressure from 1.017 MPa was able to be noticed. This is assumed to be precisely when the audible "tick" was heard. The drop in pressure was associated with a sudden deformation of the burst disk which would cause both the noise and a small increase in system volume thus reducing pressure. Upon removal from the test fixture, the electrical connection between the perforated plate and the burst disk was observed to be broken as indicated by two small holes near the foil tab. This is shown in Figure 4.3(b). While electrical continuity between the foil tab and the positive terminal is critical for normal battery operation, there was no continuity when checked with a digital multimeter after testing. As such, the audible response from the vent caps during burst pressure testing is the instant when the CID breaks and the battery would fail electrically as an open-loop.

4.1.4   High speed imaging of vent cap failures

Two tests were performed to provide a visual reference to the vent cap opening process. The first trial was using the burst pressure testing fixture to fail an MTI vent cap with the same process for all other burst tests. The second trial involved imaging more of the burst disk by testing an MTI cap with the positive terminal electrical connection removed. Figure 4.4 shows how the burst pressure test fixture was repositioned on the optical table in the testing room to allow for high speed imaging. A Photron SA-X2 with a fixed 55 mm focal length lens was arranged to directly image the vent cap through the exit of the 7/8-14 UNF coupling nut. Illumination was provided by a Fostec fiber optic ring light placed over the end of the camera lens. Both tests were recorded at frame rates of 100 kHz with a 1 μs exposure. The unmodified vent cap in Figure 4.5 was recorded with an aperture of f/2.8. The vent cap with exposed burst disk in Figure 4.6 used a setting of f/4 to provide the necessary field of view to capture the disk detaching from the vent cap. A 12.7 mm thick clear acrylic shield was used to protect the camera, lens, and ring light from any potential projectiles or from being blown by the vented air. Synchronization between the high speed camera and the National Instruments cDAQ was not performed. While it is possible to connect the Photron and National Instruments systems for data acquisition and triggering via a 5 V TTL signal, it was not necessary in this testing because total record time on the camera was approximately 4 s. Manual triggering was performed through the Photron PFV software, and video can be roughly matched to data from the pressure transducer data trace. A gamma shift with value 0.4 was used on all images to aid visibility.
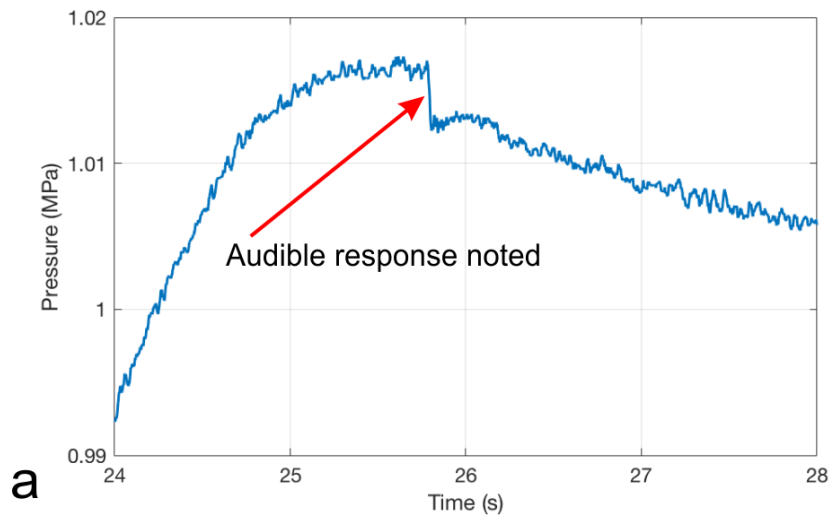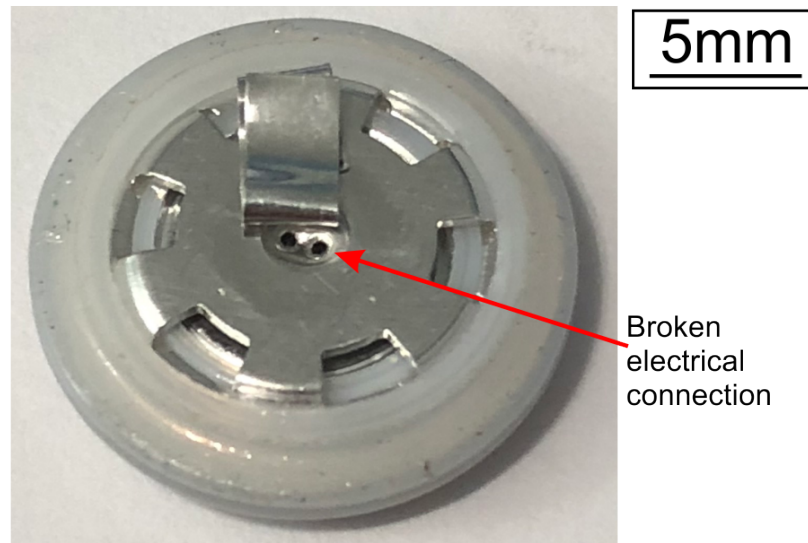
Figure 4.3: (a) Pressure trace showing slight change when audible response to the electrical failure was heard and (b) image of the vent cap after testing where the failed electrical connection is annotated.
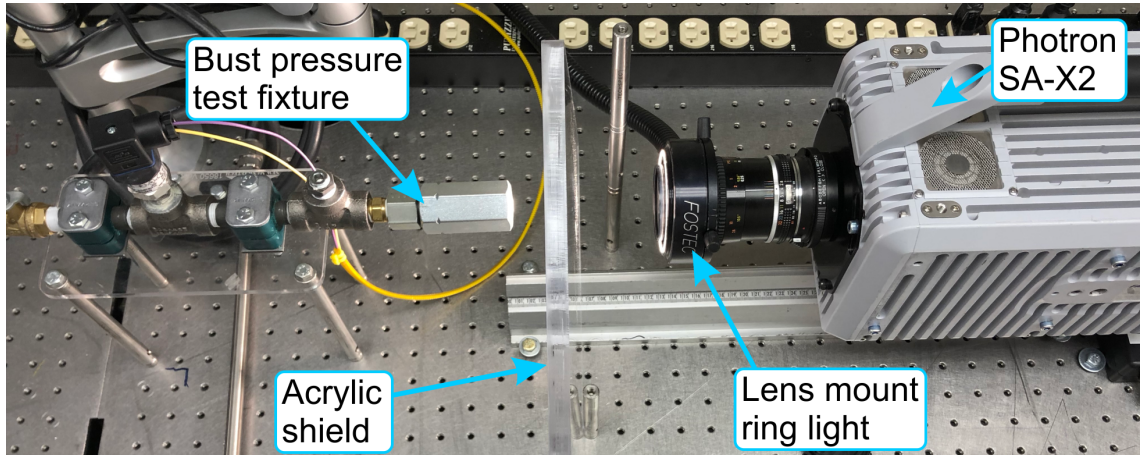
Figure 4.4: Annotated image of the modified burst pressure test setup to record high speed video of vent cap opening.

The unmodified vent cap shown in Figure 4.5 is representative of the fifty burst pressure tests of the MTI vent caps. The initial image in Figure 4.5(a) is the last image of the intact vent cap before burst disk opening was observed. A MAT-LAB script was written to highlight the changes in successive frames as compared to the initial image at $t = 0$ μs. This comparison is done via image subtraction between an image after initial opening (Figure 4.5(b) to 4.5(j)) and the initial image. Image subtraction was thresholded to show the regions where significant pixel intensity change occurred which is where the burst disk has opened along its scored perimeter. A final image closing operation was performed to connect closely spaced regions where change in the image was observed. The regions where the burst disk has opened in each image are then colored red and overlaid on the original high speed video images to provide spatial reference.

High speed imaging of the unmodified vent cap shows that there was single initial opening location which then spread circumferentially around nearly the entire scored burst disk. The perimeter of the burst disk was only visible through the four cut outs in the positive terminal which are roughly located in upper left, upper right, lower right, and lower left of the images in Figure 4.5. The first noted opening was mostly in the upper right opening and slightly in the upper left opening. The opened area spread in both directions around the circumference of the burst disk from the initial opening. After the upper right portion of the burst disk was fully open at 10 μs, the upper left was fully open at 30 μs, the lower right was fully open at 80 μs, and the lower left was mostly open at 90 μs. As the burst disk was noted to still be partially attached after the test, it can be inferred that the part of the scored disk which did not detach was on the left hand portion of the field of view.

While the unmodified MTI vent cap only showed four positions on the burst disk's circumference, the second test used a modified vent cap where the positive electrical terminal was removed. Removal of the positive terminal was
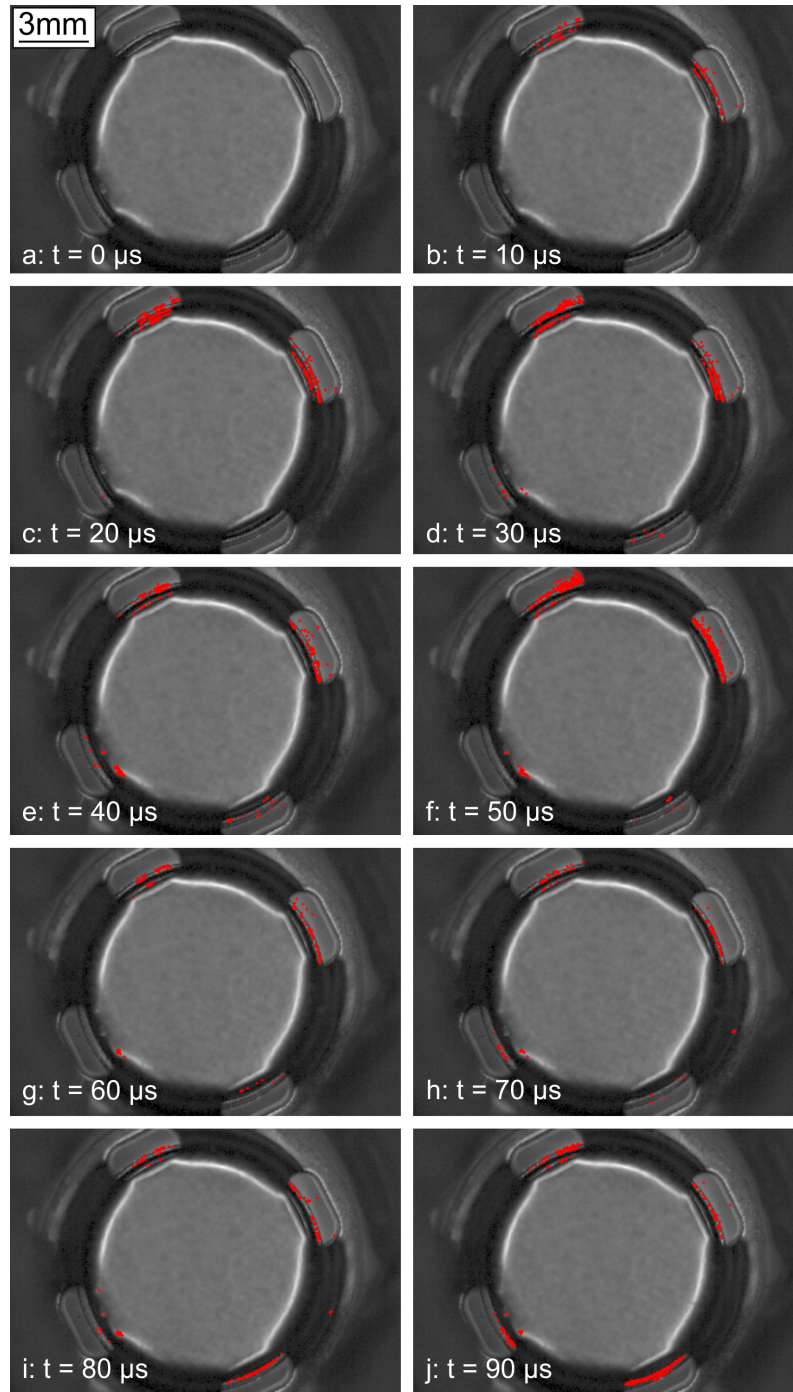
Figure 4.5: Image sequence of burst disk opening on an unmodified MTI vent cap. Changes within each frame compared to (a) immediately before burst are highlighted with red pixels. In frames (b) and (j) the opening is seen to progress around the perimeter of the scored burst disk.

performed with Dremel rotary tool and a cutting disk. Care was taken to not damage the burst disk which can be seen intact before testing in Figure 4.6(a). Early during the pressurization process of this burst test, the characteristic "tick" noise associated with electrical failure of the vent cap as described in Section 4.1.3 was observed. At this instant, the live feed from the high speed camera showed the burst disk swelling to the state seen in Figure 4.6(b) due to the connection between the center of the burst disk and the perforated plate and foil tab breaking. This swollen shape was observed from the moment the electrical connection failed to immediately before the vent cap opened. Similar to the unmodified vent cap results in Figure 4.5, the series of images recorded between $t = 40$ μs and $t = 160$ μs show that the burst disk opened at a single location and the crack spread in both directions. In this case, the two progressing edges of the crack met on the opposite side of the vent from the initial opening and led to the burst disk being completely detached. While complete disk detachment was observed with some unmodified MTI vent caps after burst testing, the lack of a positive terminal in this trial potentially made the burst disk more prone to detachment. The burst disk appeared to bend well beyond the usual constraints of the positive terminal before detachment as seen in Figure 4.6(d) and 4.6(e).
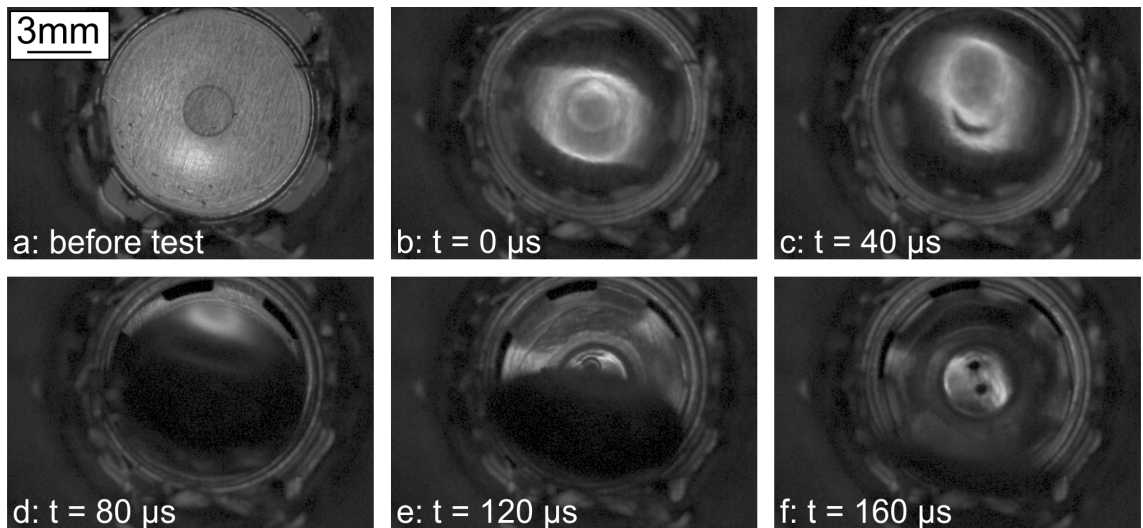
Figure 4.6: (a) Field of view showing a modified MTI vent cap with the positive electrical terminal removed to expose the burst disk and (b-f) still frames from high speed imaging at intervals of 40 μs. In frame (b), $t = 0$ μs refers to this being the last image before the burst disk begins opening.

4.2 Statistical distribution of opening area measurements

All fifty MTI vent caps used in the burst test series were retested with the COTA, and opening area calculations were made. Statistical properties of

the opening area dataset from these tests is shown in Table 4.5. The entirety of the calculated dataset is listed in Appendix B.2.1. Prior to testing, the assumed maximum possible opening area of a vent cap was set as the cross sectional area of the perforated plate on the interior side of the burst disk, but comparison between this assumed maximum of 24.98 mm^2 and the mean from the experimental dataset shows that the opening of the burst disk was significantly smaller.

Table 4.5: Statistical properties of opening area measurements

	MTI	LG
Mean	8.967 mm^2	7.025 mm^2
Minimum	7.845 mm^2	6.111 mm^2
Maximum	9.773 mm^2	7.887 mm^2
Standard deviation	0.379 mm^2	0.769 mm^2

The opening areas of the MTI vent caps show similarity to the Normal distribution as shown in Figure 4.7. The histogram was binned via the Scott method as was done for the burst pressure histogram in Figure 4.1. Table 4.6 shows the values for each of these bins. Evaluating the Normal distribution between the histogram bin limits with the calculated mean and standard deviation for the dataset gives the expected occurrences. The comparison between experimental and expected occurrences showed fair similarity to the Normal distribution, but the bin for opening areas between 9.0 mm^2 and 9.3 mm^2 was much more common than would be expected. This unexpectedly high bin would likely be suppressed if more trials were performed.

Table 4.6: Comparing MTI burst pressures to the Normal distribution

Bin range (mm^2)	Experimental occurrences	Expected occurrences
7.8 to 8.1	1	0.499
8.1 to 8.4	4	2.804
8.4 to 8.7	4	8.662
8.7 to 9.0	15	14.73
9.0 to 9.3	19	13.79
9.3 to 9.6	5	7.111
9.6 to 9.9	2	2.017
Total	50	49.61

The LG tests had statistical properties listed in Table 4.5. All tests showed opening areas smaller than the maximum opening area as represented by openings of the perforated plate which were 12.71 mm^2. The raw data from the four tests is shown in Appendix B.2.2.

In both the LG and MTI vent caps, the actual opening areas of the battery vents were much smaller than the openings in the perforated plate. The different
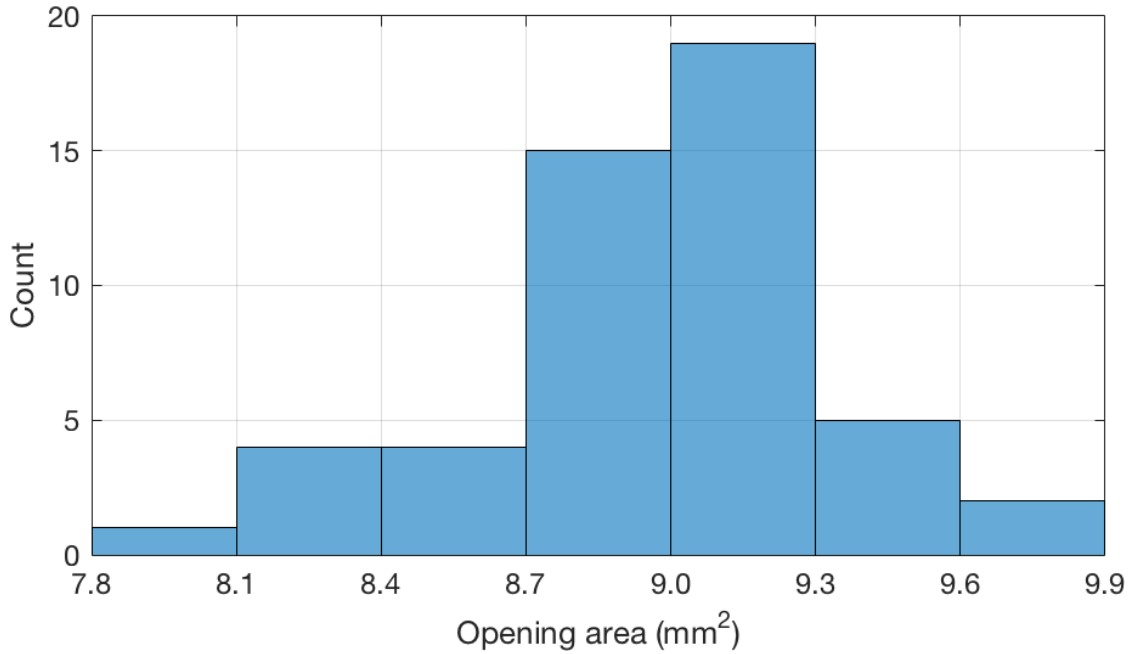
Figure 4.7: Histogram of MTI opening area data with Scott method binning

manufacturers had vent caps with significantly different perforated plates, but the opening areas were fairly similar. Even though manufacturers have different designs for the perforated plate within the battery, the feature which choked the flow was the opening around the circumference of the burst disk and the openings in the positive terminal which are very similar between cells.

4.3 Discharge coefficient calculations

4.3.1 Uncertainty analysis

Uncertainty analysis has been performed to evaluate the precision of discharge coefficient calculations. To do this, uncertainties in the accumulator tank volume (ΔV), stagnation pressure (ΔP_0), stagnation temperature (ΔT_0), and opening area (ΔA^*) were propagated through calculation uncertainty of the actual and theoretical mass flow rates as $\Delta \dot{m}_a$ and $\Delta \dot{m}_t$ respectively. Values for the gas constant and ratio of specific heats for air are assumed to be precisely known scalars within each mass flow rate equation. Error propagation equations for mass flow rate follow the standard form for propagating error through equations with parameters that are multiplied and raised to numerical exponents and are shown in Equations 4.1 and 4.2 [39].

$$\Delta \dot{m}_a = |\dot{m}_a| \sqrt{\left(\frac{\Delta V}{V}\right)^2 + \left(\frac{\Delta P_0}{P_0}\right)^2 + \left(\frac{\Delta T_0}{T_0}\right)^2} \qquad (4.1)$$

$$\Delta \dot{m}_t = |\dot{m}_t| \sqrt{\left(\frac{\Delta P_0}{P_0}\right)^2 + \left(\frac{0.5\Delta T_0}{T_0}\right)^2 + \left(\frac{\Delta A^*}{A^*}\right)^2} \qquad (4.2)$$

Since stagnation property values vary throughout testing, the uncertainty in both mass flow rates changes throughout the test. However, constant values for their uncertainties are used throughout. The uncertainty in the static and stagnation pressure measurements is chosen to be equal to the standard deviation of the noise band when measuring a constant pressure stored within the tank. This was calculated at 139 Pa when taking measurements at a rate of 1 kHz over the span of a few seconds. The uncertainty of the stagnation temperature measurement is the reported accuracy of the thermocouple by the manufacturer at 2 K [40] .

Both accumulator tank volume and vent cap opening area have constant value and uncertainty during each individual test. The accumulator tank volume was measured by filling the tank completely with water and then measuring the volume of the water. The accumulator tank had a volume of 74.3 L with an uncertainty of 0.4 L.

To calculate the uncertainty of an opening area measurement, static and stagnation pressure uncertainties were propagated through the Isentropic Flow Equations 3.1 and 3.2. Since these equations are algebraically complicated, uncertainty was propagated by for the general form of a parameter being a function of multiple other parameters. Equations 4.3 and 4.4 describe how Mach number uncertainty (ΔM_1) was first calculated from static and stagnation pressure and then propagated with uncertainty in the known cross sectional area (ΔA_1) to calculate uncertainty in choked opening area (ΔA^*). Uncertainty in the known cross sectional area was calculated 0.6 mm^2. This is equivalent to diameter variation of 0.03 mm as this was the degree of measurement on the digital calipers used to confirm the diameter of the drilled cross section. Opening area uncertainty was plotted versus time for a representative trial with an MTI brand vent cap. As shown in Figure 4.8, opening area uncertainty increased with time.

$$\Delta M_1 = \sqrt{\left(\frac{\partial M_1}{\partial P_0}\Delta P_0\right)^2 + \left(\frac{\partial M_1}{\partial P_1}\Delta P_1\right)^2} \qquad (4.3)$$

$$\Delta A^* = \sqrt{\left(\frac{\partial A^*}{\partial M_1}\Delta M\right)^2 + \left(\frac{\partial A^*}{\partial A_1}\Delta A_1\right)^2} \qquad (4.4)$$

A series of repeated trials were performed to confirm the choked opening area uncertainty calculated and represented in Figure 4.8. An acrylic circular orifice was made with a 9.44 mm^2 hole with a number 29 drill bit. Ten trials were
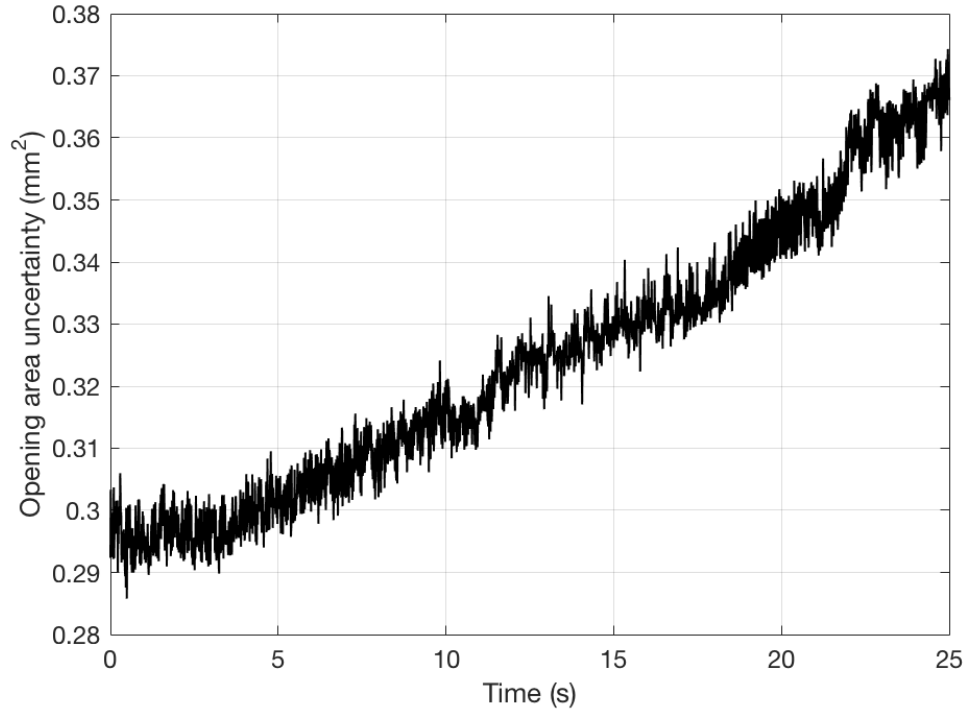
Figure 4.8: Opening area uncertainty versus time for MTI vent cap trial number 22.

performed and the results are reported in Table 4.7. The uncertainty of the repeated opening area measurements is calculated as the standard deviation of this dataset which was 0.3 mm^2 which was similar the values attained by uncertainty propagation calculations.

4.3.2 Determination of stagnation pressure range for valid discharge coefficient measurement

On all testing with 18650 battery vent caps, calculated discharge coefficient values were above unity at the beginning of tests as seen in Figure 4.9. Discharge coefficient values are reported as a function of normalized stagnation pressure here because the time scale of experiments is determined by the size of the test apparatus. However, as stagnation pressure was a monotonically decreasing parameter in all datasets, a time axis would be roughly equivalent to reading the normalized stagnation pressure from right to left. Since the actual mass flow rate can never be greater than the actual mass flow, discharge coefficient values greater than 1 are not physically possible as per Equation 3.3. This is assumed to be due to pressure and temperature measurement errors at the beginning of tests associated with time response and hysteresis in these highly transient measurements.
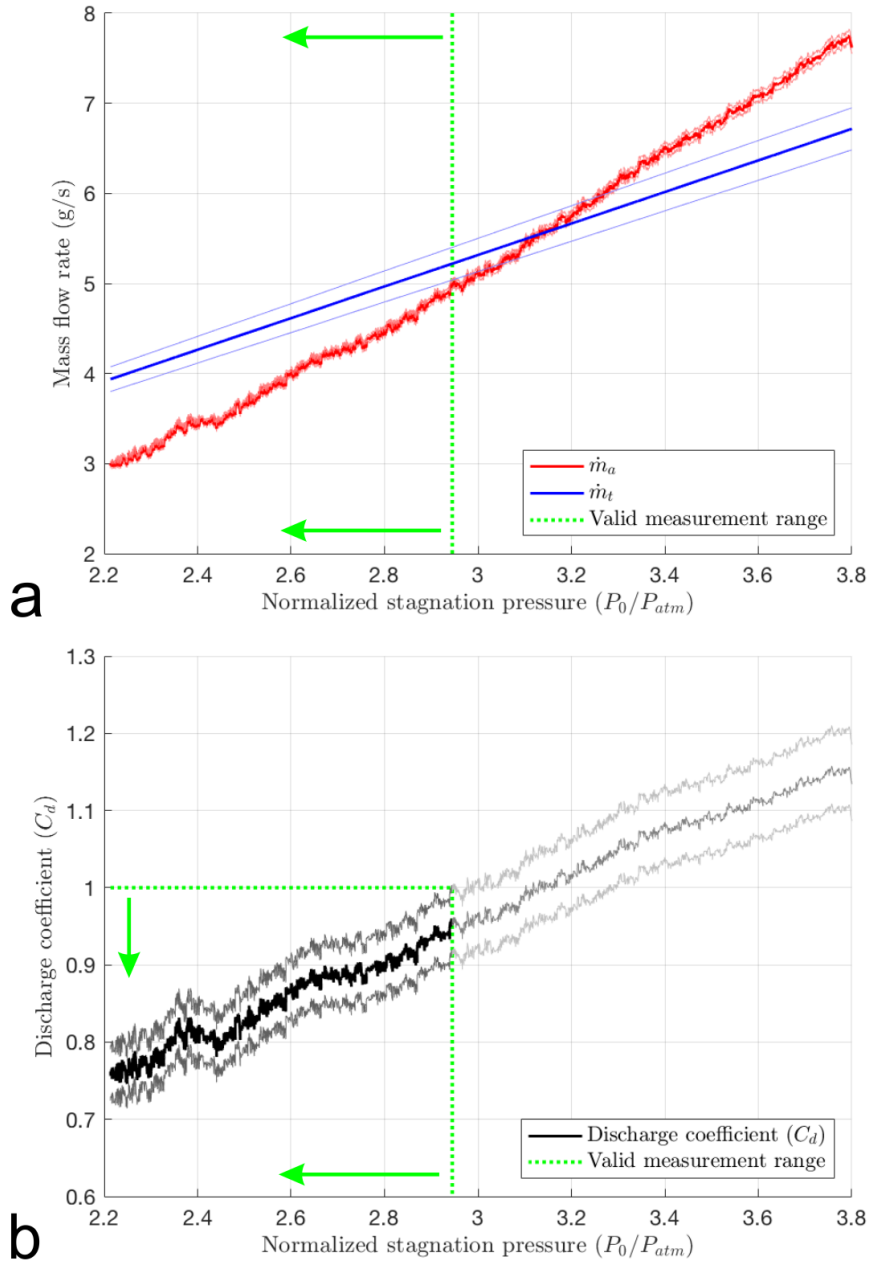
Figure 4.9: (a) Bounded actual and theoretical mass flow rates for MTI Trial 22 showing the valid measurement range, and (b) the subsequent discharge coefficient calculation plotted with upper and lower bounds.

Table 4.7: Repeated COTA testing of a Number 29 drill circular orifice

Trial number	Opening area (mm^2)
1	9.248
2	9.577
3	9.683
4	10.000
5	9.966
6	9.997
7	10.073
8	10.202
9	10.111
10	10.160

To define the region where the calculated discharge coefficient values are valid, the range of stagnation pressure values has been limited to where the largest possible actual flow rate is equal to or less than the minimum possible theoretical flow rate based on the calculated uncertainties of both parameters. Expressed mathematically, Equation 4.5 describes when the calculations are deemed valid. Graphically, the valid measurement range for a representative MTI cap was calculated to be left of the green line in Figure 4.9(a) where the bottom of the theoretical mass flow rate uncertainty band met the top of the actual mass flow rate uncertainty band.

$$\dot{m}_t - \Delta\dot{m}_t \geq \dot{m}_a + \Delta\dot{m}_a \tag{4.5}$$

Additionally, the uncertainties in mass flow rate which led to minimum and maximum possible flow rates can be used to define upper and lower bounds for discharge coefficient. Figure 4.9(b) shows how calculated discharge coefficient values from a complete test dataset for a representative MTI trial were restricted to a valid measurement range.

4.3.3 Relationship between discharge coefficient and normalized stagnation pressure

To evaluate how discharge coefficient related to stagnation pressure for the entire MTI testing series, the valid measurement range for each of the fifty trials was combined into a single dataset. The data was smoothed by calculating the mean discharge coefficient from raw data points within one hundred equal sized pressure windows between the smallest and largest valid stagnation pressures seen testing. The stagnation pressure reported for each window was the average value of its upper and lower limits. This is shown in Figure 4.10. Of note, this

data set was made to include all valid measurements, and each dataset had a unique value for the maximum normalized stagnation pressure due to variances between opened vent caps. That smallest dataset had a valid measurement range limited by a maximum normalized stagnation pressure of 2.739, on average the limit of measurement validity was $P_0/P_\text{atm} = 2.979$, and the trial went through $P_0/P_\text{atm} = 3.216$.
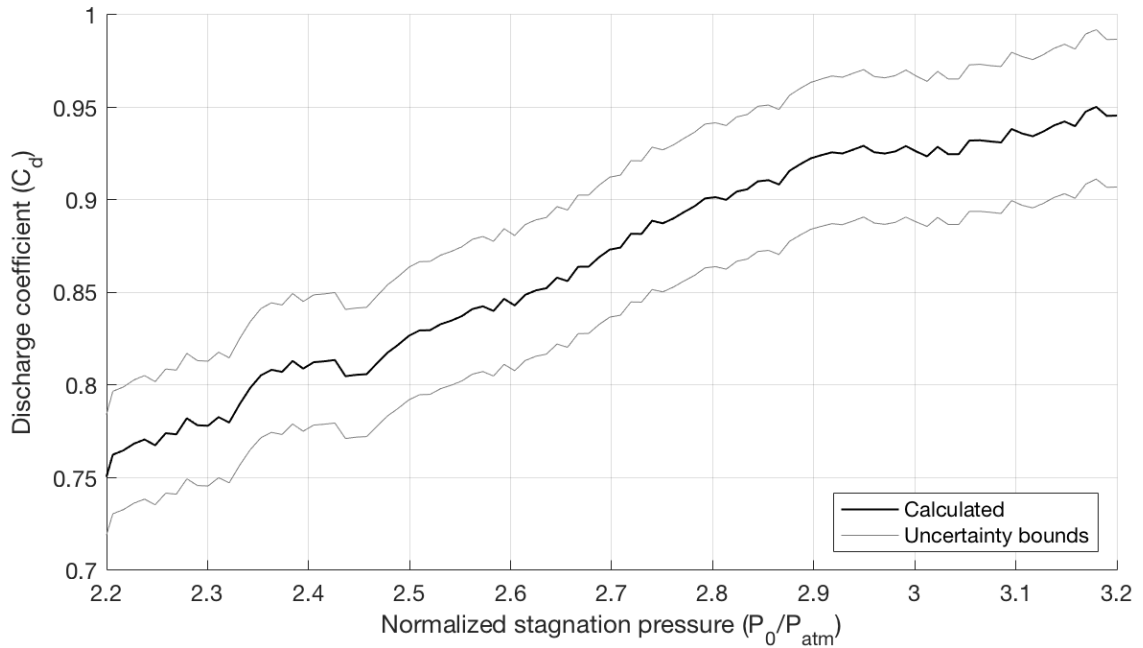
Figure 4.10: Binned and averaged values for discharge coefficient calculations from all fifty MTI vent cap tests showing the distribution of potential discharge coefficient values within the valid stagnation pressure range.

As shown in Figure 4.10, discharge coefficient consistently increased with increased normalized stagnation pressure. When $2.2 < P_0/P_\text{atm} < 2.9$, discharge coefficient increased linearly from 0.76 to 0.92. From $2.9 < P_0/P_\text{atm} < 3.2$, discharge coefficient also increased linearly at a new, decreased rate of change up to a mean value of 0.94. Small oscillations within the data were attributed to constant frequency noise bands notices in discharge coefficient calculations.

Further, discharge coefficient was plotted against time as shown in Figure 4.11. Zero time represents when the validity criteria given in Equation 4.5 for each trial was first met. Discharge coefficient values were averaged between all trials at each time step. Since trials had differing total time durations, less than the fifty total trials were averaged in later time values which was the source of increased noise after approximately 16 s. Discharge coefficient generally decreased steadily with time. The constant frequency fluctuations seen in Figure 4.10 were better defined here, and the average time between peaks is 0.55 s which correlates to a

frequency of 1.8 Hz. This 1.8 Hz frequency is assumed to be characteristic to the system itself.
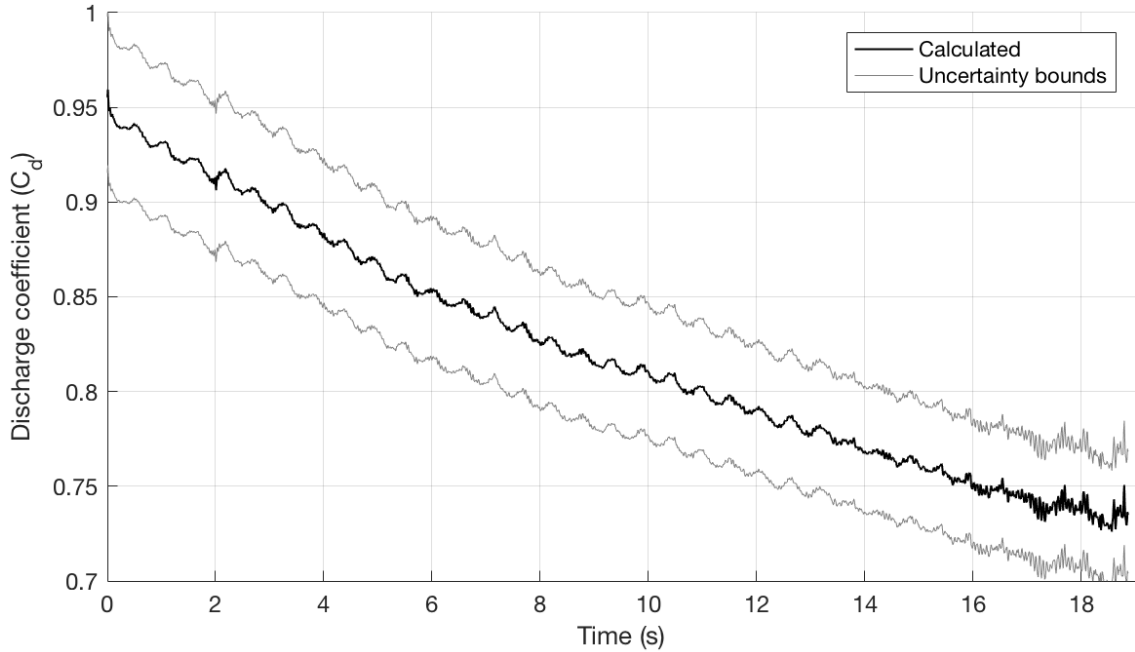
Figure 4.11: Averaged values for discharge coefficient versus time from all fifty MTI vent cap tests.

4.3.4 Statistical distribution

For statistical evaluation of the discharge coefficient distribution, a constant normalized stagnation pressure of 2.6 was chosen for comparison between individual trials. This value is in the middle the valid measurement range of all MTI vent cap datasets. The uncertainty in the discharge coefficient at this value, being the difference $C_{d,\max} - C_{d,\min}$, is 0.073 at this normalized stagnation pressure. Table 4.8 lists the calculated statistical properties, and the entire dataset is listed in Appendix B.2.1.

The histogram of the discharge coefficient data shown in Figure 4.12 indicates that the discharge coefficient values were Normally distributed. Comparison between the histogram bins and expected values from the Normal probability density function is shown in Table 4.9. Good agreement was seen between the experimental dataset and expected outcome. The difference between the mean value bin's experimental and expected occurrences can be mostly accounted for by the difference between experimental and expected values in the adjacent two

Table 4.8: Statistical properties of discharge coefficients at $P_0/P_{atm} = 2.6$

	MTI	LG
Mean	0.850	0.814
Minimum	0.788	0.801
Maximum	0.903	0.832
Standard deviation	0.024	0.014

bins. Redistribution of bin limits could potentially match the normal distribution better.
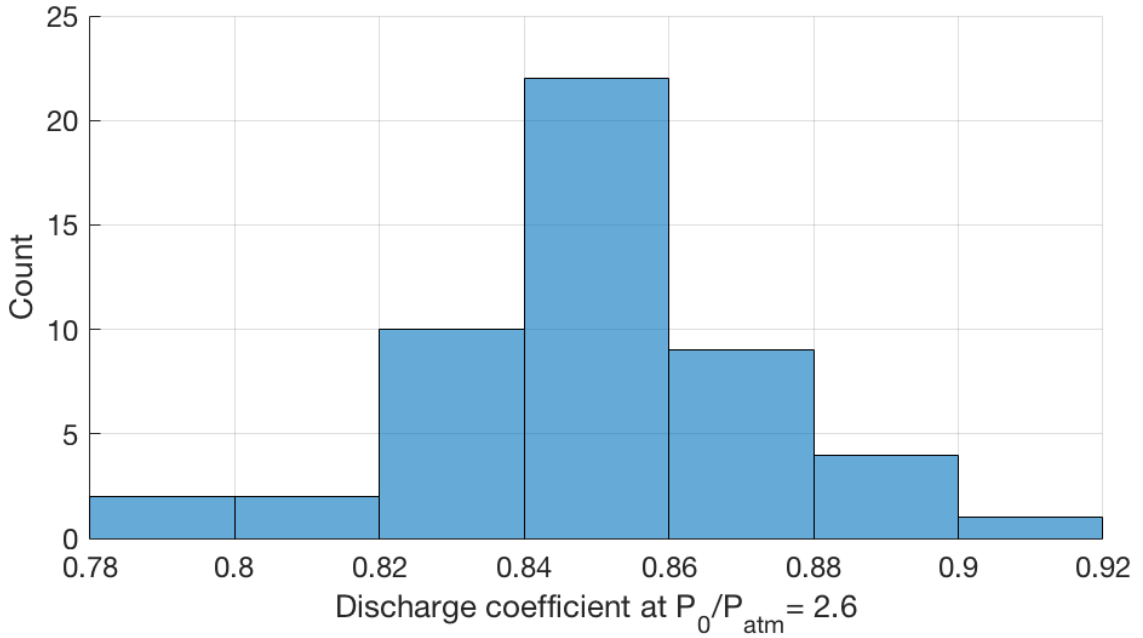
Figure 4.12: Histogram of MTI discharge coefficients at $P_0/P_{atm} = 2.6$ with Scott method binning

Discharge coefficient for the LG vent caps was also calculated at a normalized stagnation pressure. Statistical properties are shown in Table 4.8. The complete dataset is listed in Appendix B.2.2. Of note, these values for discharge coefficient were consistently lower than the MTI vent caps.

4.4 Synthesized burst pressure, opening area, and discharge coefficient results

As each vent cap was labeled and tracked throughout data analysis, vent mechanism parameters can be compared with each other between burst pressure

Table 4.9: Comparing MTI discharge coefficients at $P_0/P_{atm} = 2.6$ to the Normal distribution

Bin range (unitless)	Experimental occurrences	Expected occurrences
0.78 to 0.80	2	0.795
0.80 to 0.82	2	4.263
0.82 to 0.84	10	11.66
0.84 to 0.86	22	16.32
0.86 to 0.88	9	11.70
0.88 to 0.90	4	4.291
0.90 to 0.92	1	0.803
Total	50	49.84

measurement and COTA testing. Comparison between burst pressure, opening area, and discharge coefficients for the MTI vent cap test series shows slight or no correlation between properties. Opening area and burst pressure did not appear to show a strong correlation as seen in Figure 4.13(a), and the distribution simply reflects the spread seen in the parameters respective histograms in Figures 4.7 and 4.1.

In Figures 4.13(b) and 4.13(c), discharge coefficients recorded at a normalized stagnation pressure of 2.6 showed slightly decreasing trends with increasing opening area and discharge coefficient respectively. While increases in opening area generally correlate to increased discharge coefficient as seen in the circular orifice validation testing, more complicated orifices generally have smaller discharge coefficients. This is due to the fact that these geometries are more dissimilar to the quasi one-dimensional isentropic flow scenario used as the theoretical mass flow rate. Thus, the trend in Figure 4.13(b) can be interpreted as showing that vent caps with larger opening areas tended to have less ideal flow conditions which had a greater effect on the discharge coefficient than the increase in opening area. However, while discharge coefficient may be decreased at larger opening areas, this simply states that the efficiency of the fluid flow is further from ideal. Actual mass flow rate can be solved from a combination of Equations 3.3 and 3.4 parametrically assuming stagnation pressures and discharge coefficients are known. These two equations simplify to Equation 4.6 where mass flow rate is a function of opening area and discharge coefficient.

$$\dot{m}_a = C_d \cdot \dot{m}_t = C_d \cdot \frac{P_0}{\sqrt{RT_0}} A^* \sqrt{\gamma} \left(1 + \frac{\gamma - 1}{2}\right)^{\frac{\gamma + 1}{2 - 2\gamma}} \qquad (4.6)$$

Actual mass flow rate at a normalized stagnation pressure of 2.6 was plotted versus opening area in Figure 4.14, and shows that the mass flow rate still increases proportionally to opening area. The effect of decreased discharge coefficient values at higher opening areas is negligible in the mass flow rate as a whole.
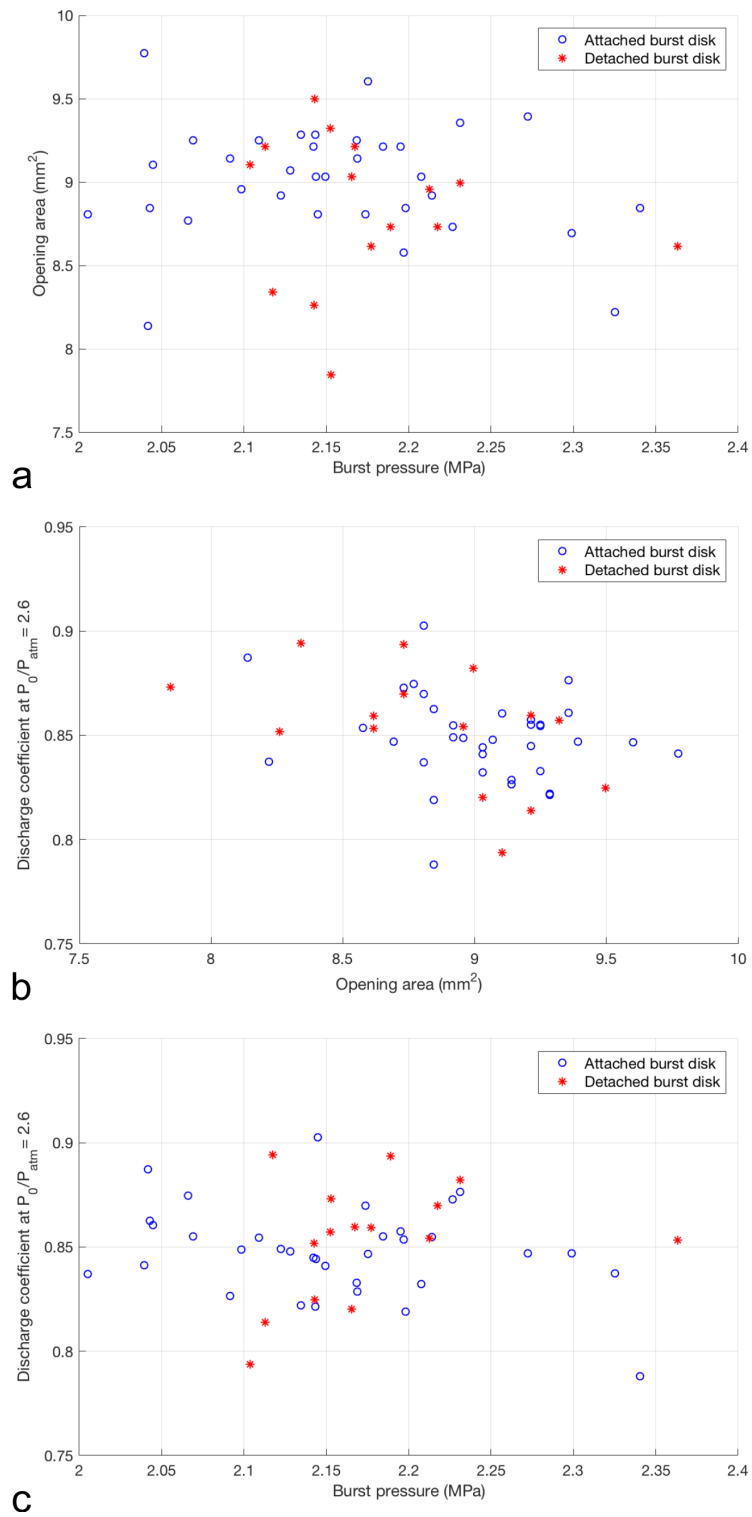
Figure 4.13: Comparing vent mechanism parameters for testing series of fifty MTI vent caps.
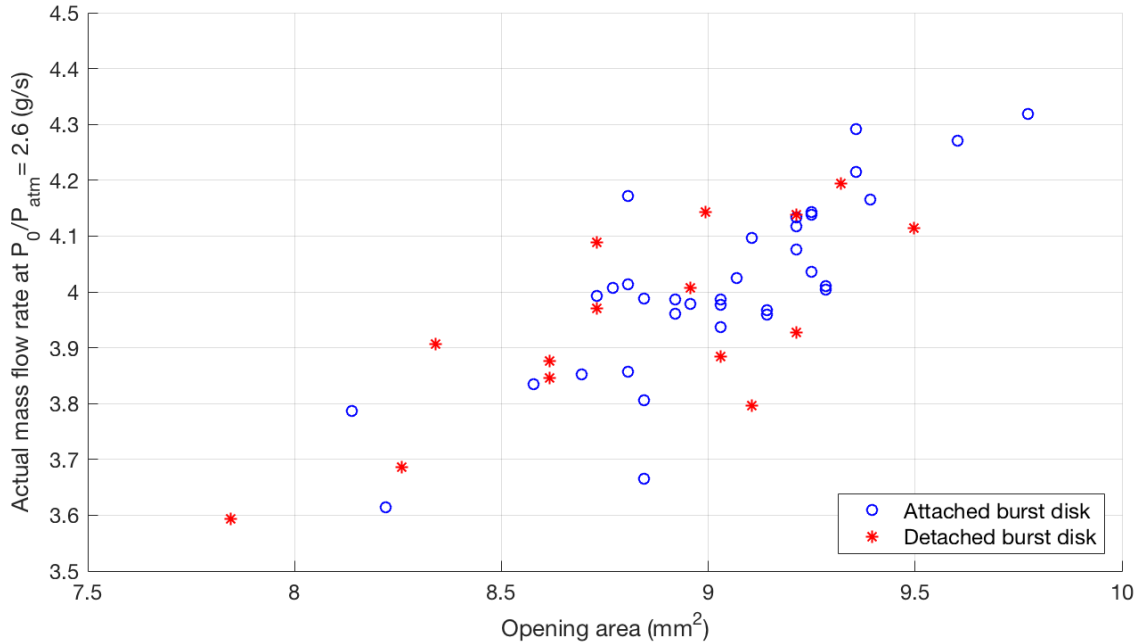
Figure 4.14: Actual mass flow rate versus opening area for testing series of fifty MTI vent caps.

A similar logic can be applied to the trend in Figure 4.13(c) where discharge coefficient decreases with increasing burst pressure. The geometry of the vent opening may become more non-ideal with more violent vent cap opening events at higher burst pressures which would have the consequence of decreased discharge coefficients.

Further, in Figures 4.13(a), 4.13(b), and 4.13(c), the vent caps with detached disks after burst testing did not appear to be distributed differently than the vent caps with attached burst disks. As shown in burst pressure measurement results, vent caps with detached burst disks showed a similar mean and standard deviation to trials with a still attached burst disk. This remains true through opening area and discharge coefficient results as shown in Table 4.10.

Table 4.10: Mean and standard deviation (STD) values for measured parameters in the MTI test series compared to attached and detached burst disk subsets

Dataset	Burst pressure (MPa)	Opening area (mm^2)	Discharge coefficient (unitless)
Complete	Mean: 2.1582	Mean: 8.967	Mean: 0.85005
	STD: 8.0953×10^{-2}	STD: 3.785×10^{-1}	STD: 2.3735×10^{-2}
Attached	Mean: 2.1504	Mean: 9.025	Mean: 0.84861
	STD: 8.6841×10^{-2}	STD: 3.361×10^{-1}	STD: 2.1308×10^{-2}
Detached	Mean: 2.1765	Mean: 8.832	Mean: 0.85342
	STD: 6.4118×10^{-2}	STD: 4.460×10^{-1}	STD: 2.9183×10^{-2}

CHAPTER 5

CONCLUSIONS

Experiments were designed and performed to measure key parameters in describing the vent mechanism present on 18650 format batteries. Vent caps were sourced commercially and removed from live batteries for these tests. A first experiment was performed to measure the burst pressure of vent caps. The COTA was developed as an experimental fixture to measure the opening area and discharge coefficient of vent caps after they have been burst open. Validation experiments with laser cut acrylic orifice plates demonstrated the accuracy of opening area measurements with the COTA for both circular openings and complicated geometries resembling the perforated plate present on all vent caps. Additional validation used precisely machined orifices of known discharge coefficient, and the calculations made from COTA measurements showed good agreement with the values described in literature. A test series of fifty commercially sourced vent caps made by MTI and another series of four vents removed from live LG brand 18650 batteries was performed. MTI testing provided statistical properties of the burst pressure, opening area, and discharge coefficient measurements and showed that all three parameters follow a Normal distribution. Additionally, mean vent parameters were different between the MTI and LG cells demonstrating the performance differences between manufacturers.

The mean burst pressure values of 2.158 MPa and 1.906 MPa for the MTI and LG cells, respectively, are significantly lower than the 3.448 MPa mentioned in literature [29]. Observations of a predictable, audible "tick" during burst pressure tests has been related to electrical disconnection of within the vent which is characteristic of CID activation. High speed imaging showed the time scale and tendency of the burst disks to open from one single point with the opening progressing in both directions around the scored line. This opening tendency can help describe the asymmetric venting seen initially in previous high speed schlieren imaging of battery failures [31].

Vent cap opening areas for both MTI and LG cells were significantly smaller than the maximum possible values if the flow was choked at the perforated plate. Also, the mean opening area for the MTI and LG vent caps were much closer to each other than their respective maximum possible values. The perforated plate geometry does not affect the sonic cross section of a vent cap. The flow will choke in the region of the vent cap around the circumference of the burst disk and the openings in the positive terminal which has a more similar geometry between manufacturers than the perforated plate.

Uncertainty analysis was used to bound the range of valid discharge coefficient measurements. Averaged experimental results from MTI trials showed discharge coefficient increasing linearly with normalized stagnation pressure with a bend in the trend at $P_0/P_{atm} = 2.9$. Discharge coefficient approachs unity at higher stagnation pressures.

While no clear correlation between burst pressure and opening area was observed when comparing measurements on a vent-by-vent basis, discharge coefficient measured at a normalized stagnation pressure of 2.6 decreases with both increased opening area and burst pressure. Even though discharge coefficient decreases at increased vent opening areas, actual mass flow rate still increased with area. Burst disk complete detachment did not appear to influence distributions of burst pressure, opening area, or discharge coefficient.

With novel quantifications of burst pressure, opening area, and discharge coefficient, the external fluid dynamics of 18650 format lithium ion battery failures can now be fully characterized in analytical and computational models on a manufacturer specific basis. Regardless of the specific abuse conditions which lead to a venting failure, the additional ability to describe how venting will occur within its surroundings will assist in the assessment of battery related hazards.

5.1 Future work

Another metric which could be quantified is the pressure at which CID activation occurs. This event was observed audibly prior to vent opening during burst pressure experiments. Whether observed via sound or electrical continuity, correlating electrical disconnection of the cell to internal pressure will provide more insight into the failures of lithium ion batteries under abuse conditions. An initial estimate for this pressure was found to be 1.017 MPa, but more statistics should be performed to assess this value.

Since experimental results have demonstrated the distribution of vent cap measurements within samples from a single manufacturer and the differences in mean values between manufacturers, these experiments should be incorporated in routine evaluation of battery vent designs. These experiments can be scaled to be effective on cylindrical cells of any size. Compiling a large database of experimentally determined burst pressure, opening area, and discharge coefficient values has the potential to be a useful resource for improving battery venting models with applications from single cells to large battery packs. The merits of different vent designs can also be objectively compared via the measured vent mechanism parameters. In a laboratory already testing the electrochemical components of commercially available cells, burst pressure and COTA experiments are simple and useful additions to battery evaluation.

APPENDIX A

NOMENCLATURE

A.1   List of symbols

Symbol	Parameter
A_1	Area at known cross section
A_e	Opening area
A^*	Sonic cross sectional area
ΔA^*	Uncertainty in A^*
C_d	Discharge coefficient
M_1	Mach number at known cross section
ΔM_1	Uncertainty in M_1
$\dot{m}$	Mass flow rate
$\dot{m}_a$	Actual mass flow rate
$\Delta \dot{m}_a$	Uncertainty in $\dot{m}_a$
$\dot{m}_t$	Theoretical mass flow rate
$\Delta \dot{m}_t$	Uncertainty in $\dot{m}_t$
P_0	Stagnation pressure (absolute)
ΔP_0	Uncertainty in P_0
P_1	Pressure at known cross section (absolute)
ΔP_1	Uncertainty in P_1
P_{atm}	Atmospheric pressure
R	Specific gas constant
T_0	Stagnation temperature
ΔT_0	Uncertainty in T_0
V	Accumulator tank volume
ΔV	Uncertainty in V
γ	Ratio of specific heats

A.2   List of abbreviations

Abbreviation	Abbreviated text

CDF	Cumulative distribution function
CID	Current interrupt device
COTA	Choked orifice testing apparatus
CT	Computed tomography
DIN	German Institute for Standardization *(translated)*
FTIR	Fourier Transform-Infrared Spectroscopy
LCO	Lithium cobalt oxide
LFP	Lithium iron phosphate
MTI	Material Technology International Corporation
NCA	Nickel-cobalt-aluminum
NI	National Instruments
NMC	Nickel-manganese-cobalt
NPT	National pipe taper
PIV	Particle image velocimetry
PTC	Positive temperature coefficient
SOC	State of charge
STD	Standard deviation
TTL	Transistor-transistor logic
UNC	Unified National Coarse Thread
UNF	Unified National Fine Thread

APPENDIX B

TABULATED EXPERIMENTAL DATA

B.1 Opening area validation experiments on the COTA

Table B.1: Experimental results from laser cut acrylic orifices

Orifice type	Actual opening area (mm^2)	Experimental opening area (mm^2)
48 Drill	3.163	3.303
44 Drill	4.014	3.872
41 Drill	4.917	4.288
38 Drill	5.376	5.280
35 Drill	6.187	7.584
28 Drill	10.00	9.974
25 Drill	11.55	11.73
21 Drill	12.73	12.99
18 Drill	14.47	15.00
15 Drill	15.88	16.85
11 Drill	18.49	19.35
8 Drill	19.57	20.67
5 Drill	21.09	22.63
2 Drill	24.19	25.59
A Drill	27.75	28.48
C Drill	30.17	30.59
E Drill	31.93	32.37
G Drill	32.82	34.18
I Drill	37.35	36.48
A123	11.23	12.25
LG	12.71	11.17
MTI	24.98	28.33
Panasonic	34.32	32.23

B.2 Burst pressure and COTA testing data

B.2.1 MTI brand commercially sourced vent caps

Table B.2: Experimental results from MTI vent caps

Trial	Burst pressure (MPa)	Disk detachment Yes/No	Opening area (mm^2)	Discharge coefficient at $P_0/P_{atm} = 2.6$
1	2.113	Yes	9.214	0.814
2	2.169	No	9.141	0.829
3	2.168	No	9.250	0.833
4	2.208	No	9.031	0.832
5	2.165	Yes	9.031	0.820
6	2.092	No	9.141	0.826
7	2.042	No	8.138	0.887
8	2.145	No	8.807	0.903
9	2.325	No	8.220	0.837
10	2.153	Yes	9.321	0.857
11	2.198	No	8.845	0.819
12	2.340	No	8.845	0.788
13	2.143	Yes	9.497	0.825
14	2.144	No	9.285	0.821
15	2.135	No	9.285	0.822
16	2.039	No	9.773	0.841
17	2.104	Yes	9.105	0.794
18	2.175	No	9.602	0.847
19	2.118	Yes	8.341	0.894
20	2.189	Yes	8.731	0.894
21	2.227	No	8.731	0.873
22	2.174	No	8.807	0.870
23	2.069	No	9.250	0.855
24	2.272	No	9.392	0.847
25	2.142	No	9.214	0.845
26	2.149	No	9.031	0.841
27	2.212	Yes	8.957	0.854
28	2.128	No	9.068	0.848
29	2.109	No	9.250	0.854
30	2.098	No	8.957	0.849
31	2.153	Yes	7.845	0.873
32	2.142	Yes	8.260	0.852
33	2.177	Yes	8.616	0.859

34	2.197	No	8.577	0.854
35	2.231	No	9.357	0.876
36	2.299	No	8.693	0.847
37	1.971	No	9.357	0.861
38	2.005	No	8.807	0.837
39	2.122	No	8.920	0.849
40	2.364	Yes	8.616	0.853
41	2.195	No	9.214	0.858
42	2.214	No	8.920	0.855
43	2.045	No	9.105	0.860
44	2.043	No	8.845	0.863
45	2.066	No	8.770	0.875
46	2.167	Yes	9.214	0.860
47	2.217	Yes	8.731	0.870
48	2.144	No	9.031	0.844
49	2.185	No	9.214	0.855
50	2.231	Yes	8.994	0.882

B.2.2 LG vent caps removed from live LG HE2 batteries

Table B.3: Experimental results from LG vent caps

Trial	Burst pressure (MPa)	Disk detachment Yes/No	Opening area (mm^2)	Discharge coefficient at $P_0/P_{atm} = 2.6$
1	1.961	No	6.111	0.832
2	1.948	No	6.740	0.806
3	1.829	No	7.360	0.801
4	1.887	No	7.887	0.816

BIBLIOGRAPHY

[1] S Abada et al. Safety focused modeling of lithium-ion batteries: A review. *Journal of Power Sources*, 306:178–192, 2016.

[2] Phillip Weicker. *A Systems Approach to Lithium-Ion Battery Management*. Artech House, 2014.

[3] Q. Wang et al. Thermal runaway caused fire and explosion of lithium ion battery. *Journal of Power Sources*, 208:210:224, 2012.

[4] E. P. Roth et al. Advanced technology development program for lithium-ion batteries: Thermal abuse performance of 18650 li-ion cells. Technical Report SAND2004-0584, Sandia National Laboratories, 2004.

[5] S. S. Zhang. Insight into the gassing problem of li-ion battery. *Frontiers in Energy Research*, 2:1–4, 2014.

[6] Engineering and safety center technical bulletin. Technical Report No. 09-02, NASA, 2009.

[7] C. Mikolajczak et al. *Lithium-Ion Batteries Hazard and Use Assessment*. Springer, 2011.

[8] P. G. Balakrishnan, R. Ramesh, and T. Prem Kumar. Safety mechanisms in lithium-ion batteries. *Journal of Power Sources*, 155:401–414, 2006.

[9] T. Unkelhaeuser and D. Smallwood. United states advanced battery consortium electrochemical storage system abuse test procedure manual. Technical Report SAND99-0497, Sandia National Laboratories, 1999.

[10] W. C. Chen et al. Effects of thermal hazard on 18650 lithium-ion battery under different states of charge. *J Therm Anal Calorim*, 121:525–531, 2015.

[11] R. E. Lyon and R. N. Walters. Energetics of lithium ion battery failure. *Journal of Hazardous Materials*, 318:164–172, 2016.

[12] Y Fu et al. An experimental study on burning behaviors of 18650 lithium ion batteries using a cone calorimeter. *Journal of Power Sources*, 273:216–222, 2015.

[13] D. P. Finegan et al. In-operando high-speed tomography of lithium-ion batteries during thermal runaway. *Nature Communications*, 2015.

[14] J. Lamb and C. J. Orendorff. Evaluation of mechanical abuse techniques in lithium ion batteries. *Journal of Power Sources*, 247:189–196, 2014.

[15] H. Wang et al. Mechanical abuse simulation and thermal runaway risks of large- format li-ion batteries. *Journal of Power Sources*, 342:913–920, 2017.

[16] H. Huang et al. Lithium metal phosphates, power and automotive applications. *Journal of Power Sources*, 189:748–751, 2009.

[17] X. Liu et al. Heat release during thermally-induced failure of a lithium ion battery: Impact of cathode composition. *Fire Safety Journal*, 85:10–22, 2016.

[18] A. W. Golubkov et al. Thermal-runaway experiments on consumer li-ion batteries with metal-oxide and olivin-type cathodes. *RSC Advances*, 4:3633–3642, 2014.

[19] Q. Wang et al. Combustion behavior of lithium iron phosphate battery induced by external heat radiation. *Journal of Loss Prevention in the Process Industries*, 49:961–969, 2017.

[20] F. Larsson et al. Characteristics of lithium-ion batteries during fire tests. *Journal of Power Sources*, 271:414–420, 2014.

[21] B. L. Ellis et al. A multifunctional 3.5 v iron-based phosphate cathode for rechargeable batteries. *Nature Materials*, 6:749–753, 2007.

[22] P. Ping et al. Study of the fire behavior of high-energy lithium-ion batteries with full-scale burning test. *Journal of Power Sources*, 285:80–89, 2015.

[23] N. S. Spinner et al. Physical and chemical analysis of lithium-ion battery cell-to-cell failure events inside custom fire chamber. *Journal of Power Sources*, 279:713–721, 2015.

[24] P. T. Coman et al. Numerical analysis of heat propagation in a battery pack using a novel technology for triggering thermal runaway. *Applied Energy*, 203:189–200, 2017.

[25] J. Lamb et al. Failure propagation in multi-cell lithium ion batteries. *Journal of Power Sources*, 283:517–523, 2015.

[26] S. Hong et al. Design of flow configuration for parallel air-cooled battery thermal management system with secondary vent. *International Journal of Heat and Mass Transfer*, 116:1204–1212, 2018.

[27] J. Xu et al. Prevent thermal runaway of lithium-ion batteries with minichannel cooling. *Applied Thermal Engineering*, 110:883–890, 2017.

[28] S. Wilke et al. Preventing thermal runaway propagation in lithium ion battery packs using a phase change composite material: An experimental study. *Journal of Power Sources*, 340:51–59, 2017.

[29] I. Buchmann. *Batteries in a Portable World a Handbook on Rechargeable Batteries for Non-Engineers*. Cadex Electronics Inc, 2001.

[30] P. T. Coman, S. Rayman, and R. E. White. A lumped model of venting during thermal runaway in a cylindrical lithium cobalt oxide lithium-ion cell. *Journal of Power Sources*, 307:56–62, 2016.

[31] F. A. Mier et al. Overcharge and thermal destructive testing of lithium metal oxide and lithium metal phosphate batteries incorporating optical diagnostics. *Journal of Energy Storage*, 13:378–386, 2017.

[32] G.S. Settles. *Schlieren and Shadowgraph Techniques*. Springer Berlin Heidelberg, 1st edition, 2001.

[33] MTI Corp. 18650 cylinder cell case with anti-explosive cap and insulation o-ring - 100 pcs/package - eq-lib-18650, 2013.

[34] H. Barkholtz et al. Multi-scale thermal stability study of lithium-ion batteries as a function of chemistry and state of charge. In *Peer Review*, 2017.

[35] J. E. John and T. G. Keith. *Gas Dynamics*. Pearson Prentice Hall, 3 edition, 2006.

[36] Y. A. Cengel and J. M. Cimbala. *Fluid Mechanics Fundamentals and Applications*. McGraw Hill, 2 edition, 2010.

[37] J. C. Kayser and R. L. Shambaugh. Discharge coefficients for compressible flow through small-diameter orifices and convergent nozzles. *Chemical Engineering Science*, 46(7):1697–1711, 1990.

[38] D. W. Scott. On optimal and data-based histograms. *Biometrika*, 66(3):605–610, 1979.

[39] J. R. Taylor. *An introduction to error analysis*. University Science Books, 1997.

[40] Omega. Wire color codes and limits of error, 2018.

MEASUREMENT OF 18650 FORMAT LITHIUM ION BATTERY VENT
MECHANISM FLOW PARAMETERS

by

FRANK AUSTIN MIER